

**Solar Models: current epoch and time dependences, neutrinos,
and helioseismological properties**

John N. Bahcall

Institute for Advanced Study, Olden Lane, Princeton, NJ 08540, U. S. A.

M. H. Pinsonneault

Department of Astronomy, Ohio State University, Columbus, Ohio 43210, U. S. A.

Sarbani Basu

Astronomy Department, Yale University, P.O. Box 208101, New Haven, CT 06520-8101,
U.S.A.

Received _____; accepted _____

ABSTRACT

We contrast the neutrino predictions from a set of eight standard-like solar models and four deviant (or deficient) solar models with the results of solar neutrino experiments. We also present the time dependences of some of the principal solar quantities that may lead ultimately to observational tests of the predicted time evolution by studying solar-type stars of different ages. In addition, we compare the computed sound speeds with the results of p -mode observations by BiSON, GOLF, GONG, LOWL, and MDI instruments. For solar neutrino and for helioseismological applications, we present present-epoch numerical tabulations of characteristics of the standard solar model as a function of solar radius, including the principal physical and composition variables, sound speeds, and neutrino fluxes.

Subject headings:

1. Introduction

Why are new calculations of standard solar models of interest? After all, solar models have been used to calculate neutrino fluxes since 1962 (Bahcall, Fowler, Iben, & Sears 1963) and p -mode oscillation frequencies since 1970 (Ulrich 1970; Leibacher & Stein 1971). Over the past four decades, the accuracy with which solar models are calculated has been steadily refined as the result of increased observational and experimental information about the input parameters (such as nuclear reaction rates and the surface abundances of different elements), more accurate calculations of constituent quantities (such as radiative opacity and equation of state), the inclusion of new physical effects (such as element diffusion), and the development of faster computers and more precise stellar evolution codes.

Solar models nevertheless remain at the frontiers of two different scientific disciplines, solar neutrino studies and helioseismology. In an era in which many major laboratory studies are underway to study neutrino oscillations with the aid of very long baselines, $\sim 10^3$ km, between accelerator and detector, solar neutrinos have a natural advantage, with a baseline of 10^8 km (Pontecorvo 1968). In addition, solar neutrinos provide unique opportunities for studying the effects of matter upon neutrino propagation, the so-called MSW effect (Wolfenstein 1978, Mikheyev & Smirnov 1985), since on their way to terrestrial detectors they pass through large amounts of matter in the sun and, at night, also in the earth .

In this paper, we provide new information about the total solar neutrino fluxes and the predicted neutrino event rates for a set of standard and non-standard solar models. Using the best-available standard solar model, we also present the calculated radial dependence of the production rate for each of the important solar neutrino fluxes. We publish for the first time the results of a precision calculation with the standard solar model of the electron density throughout the sun, from the innermost regions of the solar core to the solar atmosphere. These quantities are important for precision studies of neutrino oscillations using solar neutrinos.

We also provide detailed predictions for the time evolution of some of the important solar characteristics such as the depth and mass of the solar convective zone, the radius and the luminosity of the sun, the central temperature, density, pressure, and hydrogen mass fraction, as well as the temperature, density, pressure, and radiative opacity at the base of the convective zone. As far as we know, these are the first detailed results submitted for publication on the time evolution of many of these quantities. Some of the calculated time dependences may be subject to observational tests.

At the present writing, the sun remains the only main-sequence star for which p-mode

oscillations have been robustly detected. Thus only for the sun can one measure precisely tens of thousands of the eigenfrequencies for stellar pressure oscillations. The comparison between the sound speeds and pressures derived from the observed p-mode frequencies and those calculated with standard solar models has provided a host of accurate measurements of the interior of the nearest star. The solar quantities determined by helioseisology include the sound velocity and density as a function of solar radius, the depth of the convective zone, the interior rotation rate, and the surface helium abundance. The excellent agreement between the helioseismological observations and the solar model calculations has shown that the large discrepancies between solar neutrino measurements and solar model calculations cannot be due to errors in the solar models (cf. Figure 10).

In this paper, we present a refined comparison between our best standard solar model and measurements of the solar sound speeds obtained using oscillation data from a number of different sources. We use a combination of data from the LOWL instrument and the BiSON network, two sets of data from the GOLF instrument, as well as data from the GONG network and the MDI instrument.

We describe in the following paragraph the organization of this paper. But, since this paper contains a lot of information on disparate topics, we recommend that the reader first turn to the final section, § 8, and peruse our summary and discussion of the main new results. Section 8 may help the reader decide which sections of the paper the reader wants to read (or to skip). The different sections are written so that they can be read more or less independently.

Section 2 defines the slightly-improved Standard solar model and describes the numerical tables that present details of the contemporary characteristics of the Standard model. Section 3 describes the main sequence time dependences of some of the most important characteristics of the Standard model. We present in this section the time

evolution of the solar radius and luminosity, the properties of the convective zone, and the physical characteristics of the center of the sun. We discuss solar properties from the initial age main sequence to an age of 8 billion years. Section 4 defines and compares the physical characteristics of seven variant standard models and four deviant (deficient) solar models, which together with the Standard model make up a set of twelve models whose neutrino fluxes we evaluate in this paper. We previously used a subset of nine of these models to test the robustness of helioseismological inversions (Basu, Pinsonneault, & Bahcall 2000, hereafter BPB2000). We discuss in this same section two new standard-like solar models with heavy element to hydrogen ratios that differ slightly from our previously adopted value of Z/X . Section 5 discusses solar neutrino physics. We present the predicted present-day neutrino fluxes for the Standard model and for all of the variant and deviant solar models, as well as the electron number density versus solar radius. We contrast the predicted neutrino event rates with the results of the chlorine, Kamiokande, GALLEX, SAGE, SuperKamioKande, and GNO solar neutrino experiments. We also give in this section the calculated time evolution of the most important solar neutrino fluxes. Section 6 compares calculated and observed sound speeds. We present the results both on a panoramic scale suitable for discussing the implications for solar neutrino physics and on a zoomed-in scale appropriate for detailed investigations of solar physics. In § 7, we compare, for all 12 of the solar models discussed in this paper, the calculated values of the surface helium abundance and the depth of the convective zone with the measured values for these quantities. We summarize and discuss our main results in § 8.

2. Standard solar model

We define in § 2.1 the Standard solar model and present in § 2.2 some of the important contemporary characteristics of the Standard solar model, including detailed tables of the

physical variables as a function of the solar radius.

By ‘Standard solar model’, we mean the solar model which is constructed with the best-available physics and input data. Naturally, Standard models improve with time, as the input data are made more accurate, the calculational techniques become faster and more precise, and the physical description is more detailed. Thus it is necessary at each presentation of a new Standard model to describe what has changed from the previous best model and to provide references to the earlier work. The reader can see Bahcall (1989) for a general reference to the early work on precise solar models that were motivated by the need to predict accurate solar neutrino fluxes and to make comparisons with helioseismological data.

2.1. Definition of the Standard model

Our standard solar model¹ is constructed with the OPAL equation of state (Rogers, Swenson & Iglesias 1996) and OPAL opacities (Iglesias & Rogers 1996), which are supplemented by the low temperature opacities of Alexander & Ferguson (1994). The model was calculated using the usual mixing length formalism to determine the convective flux.

The principal change in the input data is the use of the Grevesse & Sauval (1998) improved standard solar composition. The refinements in this composition redetermination come from many different sources, including the use of more accurate atomic transition probabilities in interpreting solar spectra.

¹To simplify the language of the discussion, we will often describe characteristics of the Standard model as if we knew they were characteristics of the sun. Following common practice in the literature, we will sometimes abbreviate the reference to this Standard model as BP2000 or Bahcall-Pinsonneault 2000.

The nuclear reaction rates were evaluated with the subroutine `exportenergy.f` (cf. Bahcall & Pinsonneault 1992), using the reaction data in Adelberger et al. (1998) and with electron and ion weak screening as indicated by recent calculations of Gruzinov & Bahcall (1998); see also Salpeter (1954). The model incorporates helium and heavy element diffusion using the exportable diffusion subroutine of Thoul (cf. Thoul, Bahcall & Loeb, 1994; Bahcall & Pinsonneault 1995)². We have used the most recent and detailed calculation (Marcucci et al. 2000a) for the S_0 -factor for the ${}^3\text{He}(p, e^+ + \nu_e){}^4\text{He}$ reaction: $S_0(\text{hep}) = 10.1 \times 10^{-20}$ keV b, which is a factor of 4.4 times larger than the previous best-estimate (see § 5.1.2 and Bahcall & Krastev 1998, Marcucci et al. 2000b for a discussion of the large uncertainties in calculating $S_0(\text{hep})$). For values of $S_0(\text{hep})$ in the range of current estimates, the assumed rate of the *hep* reaction only affects in a noticeable way the calculated flux of *hep* neutrinos and does not affect the calculated fluxes of other neutrinos, the helioseismological characteristics, or other physical properties of the sun.

For the standard model, the evolutionary calculations were started at the main-sequence stage. The model has a radius of 695.98 Mm. We do not study the pre-main sequence evolution in our standard model. This epoch has been discussed in the classical work of Iben (1965) and the effects of pre-main sequence have been shown by Bahcall & Glasner (1994) to be unimportant for solar neutrino calculations (see also the thorough discussion by Morel, Provost, & Berthomieu 2000). We do consider one pre-main sequence model, which differs very little from the corresponding model started at the zero-age main sequence.

The ratio of heavy elements to hydrogen (Z/X) at the surface of the model is 0.0230, which was chosen to be consistent with the value obtained by Grevesse & Sauval (1998). A

²Both the nuclear energy generation subroutine, `exportenergy.f`, and the diffusion subroutine, `diffusion.f`, are available at the Web site www.sns.ias.edu/~jnb, menu item: neutrino software and data.

Krishnaswamy T - τ relationship for the atmosphere was used. We adopt a solar luminosity $L_{\odot} = 3.844 \times 10^{33}$ erg s⁻¹ and a solar age of 4.57×10^9 yr (see Bahcall & Pinsonneault 1995).

In the course of our recent analysis of systematic uncertainties in helioseismological inversions (Basu, Pinsonneault, & Bahcall 2000), we uncovered an error in our code for the interpolation of the OPAL 95 opacities. The edges of opacity tables were flagged by zero opacity values; unfortunately, there were some interpolation problems associated with the occurrence of zero values inside the table. This problem occurred because the logarithm of the opacity, which is what we were tabulating, can actually be zero. The interpolation error caused small changes in the opacity which produced errors in the sound speed of order 0.1% for solar radii in the range of $0.3R_{\odot}$ to $0.7R_{\odot}$ and errors of order 3% in the ⁸B neutrino flux (with smaller errors for other neutrino fluxes). In the following sections, we will point out more specifically the changes in the neutrino predictions and in the sound velocities that are produced by correcting this interpolation error. These changes are particularly apparent in the comparison of Figure 12 and Figure 13, which are discussed in the helioseismology section, § 6.

2.2. Some contemporary characteristics of the standard solar model

The details of the structure of a standard solar model are of importance for both helioseismology and solar neutrino calculations. In the first paper in this series in which we published the details of a model of the solar interior structure (Bahcall et al. 1982), we presented a table with only 27 radial shells (rows of numbers) and 10 variables for each shell (mass, radius, temperature, density, hydrogen fraction, helium fraction, luminosity generated, and the source density of the $p-p$, ⁷Be, and ⁸B neutrinos). Over the years, much greater precision was required by the increasing sophistication of the helioseismological

measurements and the solar neutrino calculations. Fortunately, the computing capacity more than made up for the necessary increase in model details.

We have created from the output of the present calculations two exportable computer files that contain in easily readable form the details of our best Standard solar model (BP2000). Physical variables are given at 875 separate radial shells. In addition to the variables cited above, this file contains the pressure, electron number density, the mass fractions of ^3He , ^7Be , ^{12}C , ^{14}N , and ^{16}O , as well as the source densities of all eight of the most important solar neutrino fluxes. These files are accessible at <http://www.sns.ias.edu/~jnb>. Previous standard solar models in this series (published in 1982, 1988, 1992, 1995, as well as 1998) are available at the same URL and can be used to test the robustness of conclusions that depend upon models of the solar interior.

3. Time dependences

In this section, we present and discuss the time dependences of some of the principal characteristics of the standard solar model. We begin in § 3.1 by describing the separate temporal evolution of the solar radius and the solar luminosity and then discuss the simple relation we have found between the values of these two quantities as a function of time. We also demonstrate that the solar luminosity is a robust function of time. In § 3.2, we present the time-dependent fractions of the solar luminosity that are produced by different nuclear fusion reactions. We concentrate in § 3.3 on the convective zone, presenting the calculated time dependences of the depth and the mass of the convective zone. We also report the time dependence of the temperature, density, pressure, and opacity at the base of the convective zone. In § 3.4, we discuss the time dependence of quantities at the center of the sun, the central temperature, density, pressure, and hydrogen mass fraction. Since we do not discuss pre-main sequence evolution, our calculations are not precise for times less than 0.1×10^9 yr

(see Morel et al. 2000; Weiss and Schlattl 1998).

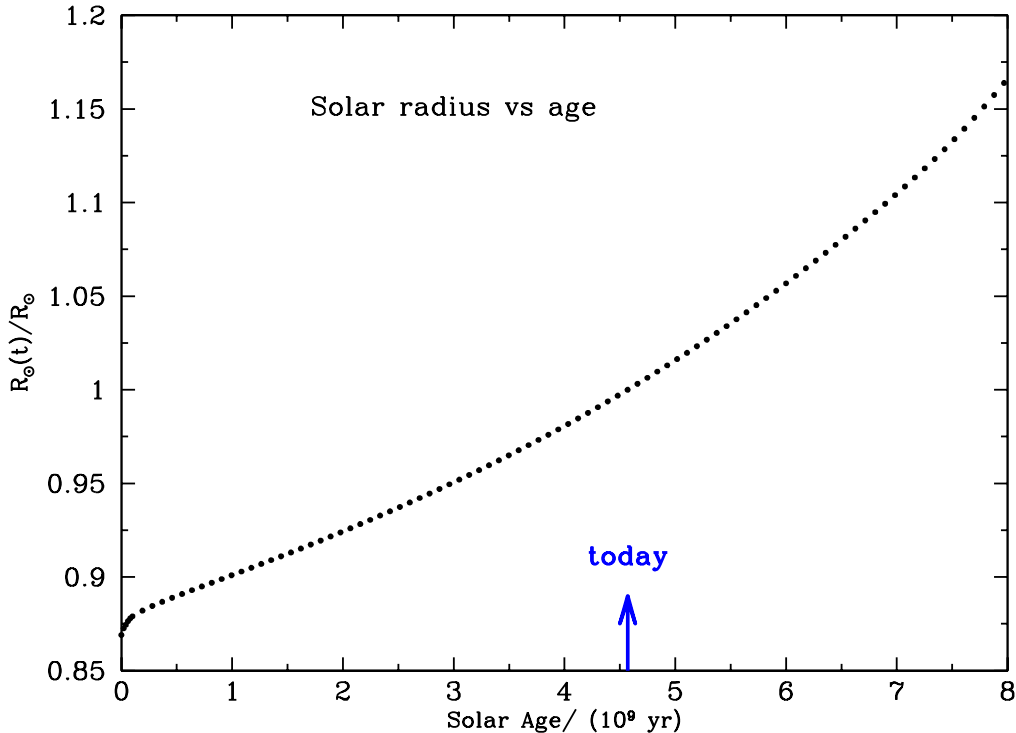


Fig. 1.— The calculated radius, $R_{\odot}(t)$, as a function of age for the standard solar model, Bahcall-Pinsonneault 2000. The solar age is measured in units of 10^9 yr. The present age of the sun, 4.57×10^9 years, is indicated by an arrow in Figure 1. The radius increases from $0.87R_{\odot}$ at the zero age main sequence to $1.0R_{\odot}$ at the present epoch and $1.18R_{\odot}$ at a solar age of 8 billion years.

3.1. Radius and luminosity versus age

Figure 1 and Table 1 present the calculated radius of the sun versus solar age for the standard solar model. The values given are normalized to the present-day solar radius, R_{\odot} . Over the lifetime of the sun, the model radius has increased monotonically from an initial value of $0.869R_{\odot}$ to the current value $1.0R_{\odot}$, a 15% rise. At a solar age of 8 billion years, the solar radius will increase to $1.17R_{\odot}$. We shall see in the following discussion that some of the important evolutionary characteristics of the sun can be expressed simply in terms of

Table 1: The solar radius, $R_{\odot}(t)$, as a function of solar age for the Standard solar model. The present age of the sun is 4.57×10^9 years (see Bahcall & Pinsonneault 1995)

Age (10^9 yr)	$R_{\odot}(t)$ (R_{\odot} (today))	Age (10^9 yr)	$R_{\odot}(t)$ (R_{\odot} (today))
0.0	0.869	4.2	0.987
0.2	0.882	4.4	0.994
0.4	0.888	4.6	1.001
0.6	0.892	4.8	1.008
0.8	0.897	5.0	1.016
1.0	0.901	5.2	1.023
1.2	0.906	5.4	1.031
1.4	0.910	5.6	1.040
1.6	0.915	5.8	1.048
1.8	0.920	6.0	1.057
2.0	0.924	6.2	1.066
2.2	0.929	6.4	1.075
2.4	0.934	6.6	1.085
2.6	0.940	6.8	1.095
2.8	0.945	7.0	1.105
3.0	0.951	7.2	1.116
3.2	0.956	7.4	1.127
3.4	0.962	7.6	1.139
3.6	0.968	7.8	1.152
3.8	0.974	8.0	1.166
4.0	0.981		

the ratio $R_{\odot}(t)/R_{\odot}(\text{today})$.

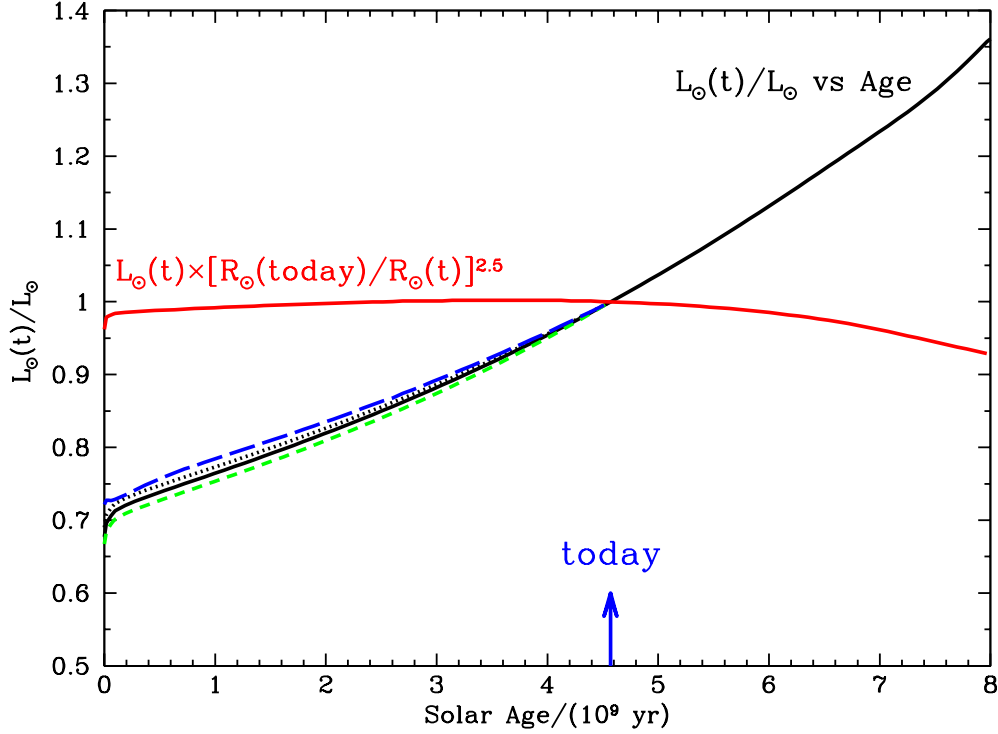


Fig. 2.— The normalized solar luminosity, $L_{\odot}(t)/L_{\odot}(\text{today})$ versus solar age for the Standard solar model (solid curve) and for three ‘deficient’ solar models: the No Diffusion model (dotted curve), the $S_{34} = 0$ model (short dashes), and the Mixed model (long dashes). The luminosity evolution of the sun is essentially the same in all solar models we have investigated, including deficient solar models. The product $L_{\odot}(t) \times R_{\odot}(t)^{-2.5}$ varies by $\pm 4\%$ over the entire period from the zero age main sequence to a solar age of 8 billion years, while the solar luminosity itself varies by slightly more than a factor of two during this period. In the period between 4 billion years to 8 billion years, the relation $L_{\odot}(t) \propto R_{\odot}(t)^2$ is satisfied to $\pm 1/2\%$. The solar luminosity has increased by 48% from the zero main sequence to the present epoch. The present age of the sun is indicated by an arrow at 4.59×10^9 years.

Figure 2 and Table 2 show the calculated solar luminosity as a function of solar age, normalized to the present-day solar luminosity, L_{\odot} . The total solar luminosity has risen monotonically from a zero-age value of $0.677L_{\odot}$. We also show in Figure 2 the solar luminosity as a function of time for three deficient solar models that are described in the following section. All of the solar models show essentially the same luminosity evolution.

Table 2: Solar luminosity as a function of solar age for the Standard solar model. The table gives the computed values of the solar luminosity in units of the present-day solar luminosity. The model was iterated to give the observed luminosity at the present epoch, 4.57×10^9 yr.

Age (10^9 yr)	$L_{\odot}(t)$ (L_{\odot} (today))	Age (10^9 yr)	$L_{\odot}(t)$ (L_{\odot} (today))
0.0	0.677	4.2	0.970
0.2	0.721	4.4	0.986
0.4	0.733	4.6	1.003
0.6	0.744	4.8	1.020
0.8	0.754	5.0	1.037
1.0	0.764	5.2	1.055
1.2	0.775	5.4	1.073
1.4	0.786	5.6	1.092
1.6	0.797	5.8	1.112
1.8	0.808	6.0	1.132
2.0	0.820	6.2	1.152
2.2	0.831	6.4	1.172
2.4	0.844	6.6	1.193
2.6	0.856	6.8	1.214
2.8	0.869	7.0	1.235
3.0	0.882	7.2	1.256
3.2	0.896	7.4	1.278
3.4	0.910	7.6	1.304
3.6	0.924	7.8	1.332
3.8	0.939	8.0	1.363
4.0	0.954		

Figure 2 shows that the product

$$L_{\odot}(t) \times R_{\odot}(t)^{-2.5} = \text{constant} \quad (1)$$

to an accuracy of about $\pm 4\%$ over the entire period from the zero age main-sequence to an age of 8 billion years. The solar luminosity $L_{\odot}(t)$ varies from $0.68L_{\odot}$ to L_{\odot} at the present epoch and will reach $1.36L_{\odot}$ after 8 billion years on the main sequence. The corresponding values of $L_{\odot}(t) \times [R_{\odot}(\text{today})/R_{\odot}(t)]^{2.5}$ are 0.96, 1.00, and 0.93. Thus the luminosity of the sun varies by slightly more than a factor of two while $L_{\odot}(t) \times [R_{\odot}(\text{today})/R_{\odot}(t)]^{2.5}$ varies by only a few percent.

Over the first 5 billion years, Eq. (1) is satisfied to an accuracy of $\pm 2\%$. From 4 billion years to 8 billion years, the relation is somewhat less steep, $L_{\odot}(t) \propto R_{\odot}(t)^2$ to an accuracy of $\pm 1/2\%$. This transition from $L_{\odot}(t) \propto R_{\odot}(t)^{2.5}$ to $L_{\odot}(t) \propto R_{\odot}(t)^2$ can be seen clearly in Figure 2.

Figure 2 shows that the evolution of the luminosity with time is robust. We have plotted in Figure 2 the time evolution of three solar models that are seriously deficient in some of the physics input, the ‘No Diffusion’, the ‘ $S_{34} = 0$ ’, and the ‘Mixed’ models. These deficient models show a luminosity evolution that is very similar to that of the standard solar model.

Table 3 gives the calculated effective temperature of the Standard model, T_{eff} , as a function of solar age. The effective temperature varies by only $\pm 1.5\%$ over the entire period from the zero age main sequence to an age of 8 billion years and only by $\pm 0.7\%$ from 2 billion years to 8 billion years. In the last four billion years shown in Table 3, the effective temperatures varies by only $\pm 0.25\%$, which reflects the scaling relation $L_{\odot}(t) \propto R_{\odot}(t)^2$ that is valid in this period.

Table 3: The calculated effective temperature as a function of solar age for the Standard model. The solar age is measured in units of 10^9 yr and the solar effective temperature is measured in units of the present-epoch effective temperature

Age	T_{eff}	Age	T_{eff}
0.0	0.973	4.5	1.000
0.5	0.983	5.0	1.001
1.0	0.985	5.5	1.002
1.5	0.987	6.0	1.003
2.0	0.990	6.5	1.003
2.5	0.992	7.0	1.003
3.0	0.994	7.5	1.001
3.5	0.996	8.0	1.000
4.0	0.998		

3.2. Energy fractions

Figure 3 shows, for the Standard model, the energy generated by different nuclear fusion reactions as a function of solar age. The present-day total solar luminosity, $L_{\odot}(\text{today})$, is the unit of luminosity in Figure 3.

The branch of the $p - p$ chain that is denoted in Figure 3 by $p - p + {}^3\text{He}-{}^3\text{He}$ (the dashed curve) proceeds primarily through the reactions $p(p, e^+ \nu_e){}^2\text{H}(p, \gamma){}^3\text{He}({}^3\text{He}, 2p){}^4\text{He}$. For simplicity, we include all $p - p$ reactions in this sum but do not show explicitly the pep reactions in the above scheme. The small energy contribution due to pep reactions is included in the calculations that led to Figure 3. The ${}^3\text{He}-{}^4\text{He}$ branch (the dot-dashed curve) includes the nuclear reactions that produce both the ${}^7\text{Be}$ and the ${}^8\text{B}$ neutrinos: ${}^3\text{He}({}^4\text{He}, \gamma){}^7\text{Be}(e^-, \nu_e){}^7\text{Li}(p, {}^4\text{He}){}^4\text{He}$ and ${}^3\text{He}({}^4\text{He}, \gamma){}^7\text{Be}(p, \gamma){}^8\text{B}({}^4\text{He} + e^+ + \nu_e){}^4\text{He}$. The CNO reactions are denoted by CNO in Figure 3.

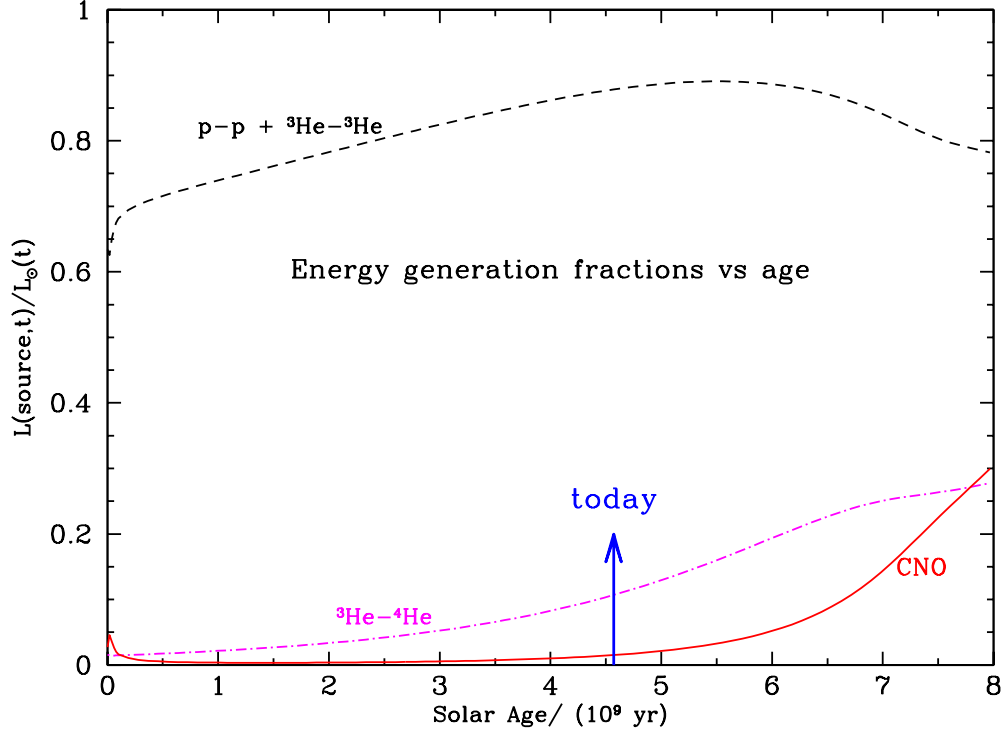


Fig. 3.— The fraction in the Standard model of the solar luminosity produced by different nuclear fusion reactions versus solar age. The luminosity generated by the $p - p$ nuclear fusion branch that is terminated by the ${}^3\text{He}-{}^3\text{He}$ reaction is marked by a dashed curve in the figure and the luminosity produced by the $p - p$ branches that proceed through the ${}^3\text{He}-{}^4\text{He}$ reaction is denoted by a dot-dashed curve. The luminosity generation by the CNO cycle is indicated by a solid line. The unit of luminosity is the present-day total solar luminosity. At the present epoch, the $p - p + {}^3\text{He}-{}^3\text{He}$ reactions produce 87.8% of the solar luminosity and the branches terminating through the ${}^3\text{He}-{}^3\text{He}$ reaction generate 10.7% of the solar luminosity. The CNO cycle produces 1.5% of the present-epoch luminosity.

The branch that terminates via the ${}^3\text{He}-{}^3\text{He}$ reaction dominates the solar energy generation throughout the main sequence lifetime shown in Figure 3, although the CNO reactions overtake the ${}^3\text{He}-{}^4\text{He}$ branches at an age of about eight billion years. At an age of one billion years, 96.7% of the solar luminosity is generated through $p - p$ reactions plus the ${}^3\text{He}-{}^3\text{He}$ termination, 2.8% through the ${}^3\text{He}-{}^4\text{He}$ termination, and only 0.5% through the CNO cycle. The situation gradually changes as the sun heats up. At the present epoch, the ${}^3\text{He}-{}^3\text{He}$ termination produces 87.8% of the solar luminosity and the branches

terminating through the ${}^3\text{He}-{}^4\text{He}$ reaction generate 10.7% of the solar luminosity. The CNO cycle produces 1.5% of the present-epoch luminosity. By the time the Standard solar model reaches an age of eight billion years, the percentages are 57.6%, 20.4%, and 22.0%, respectively, for ${}^3\text{He}-{}^3\text{He}$, ${}^3\text{He}-{}^4\text{He}$, and CNO reactions. The energy loss due to gravitational energy expansion ranges from -0.03% to -0.04% to -0.07% as the sun’s age increases from one billion years to the present epoch to eight billion years.

3.3. Convective zone

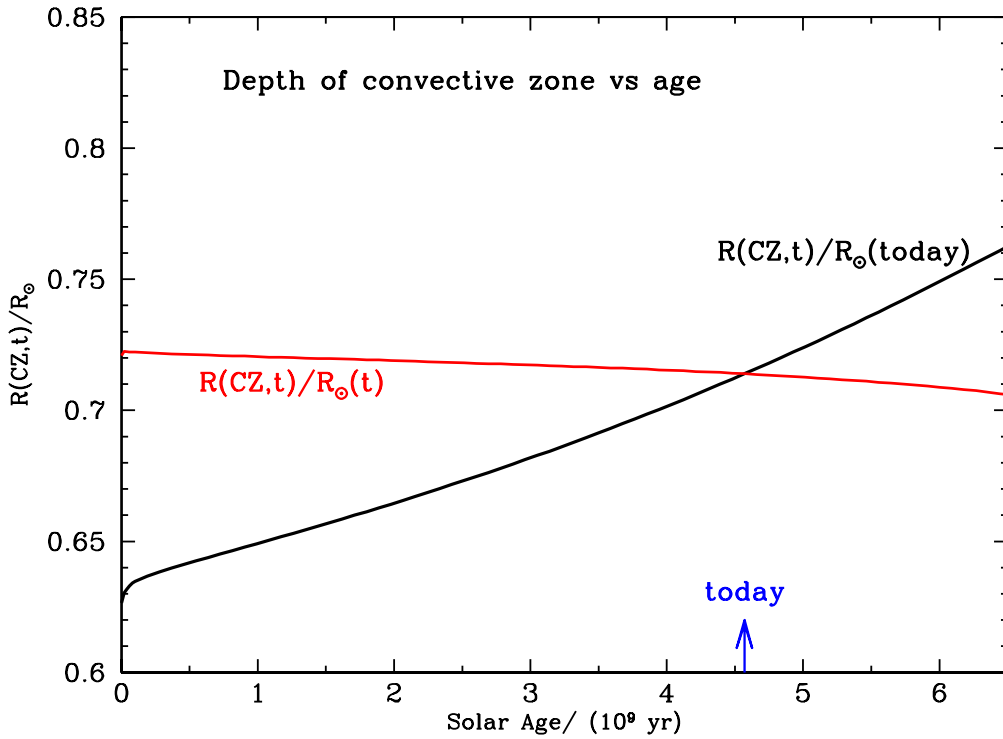


Fig. 4.— The depth of the convective zone, $R(\text{CZ}, t)$, as a function of age for the standard solar model. The depth of the convective zone is approximately proportional to the contemporary solar radius. The solar age is measured in units of 10^9 yr.

Figure 4 shows the depth of the convective zone, $R(\text{CZ}, t)$, as a function of age for the standard solar model. Correspondingly, Figure 5 shows the mass of the convective zone,

$M(\text{CZ}, t)$, as a function of age. In both cases, the temporal dependence from the zero age main sequence to the current epoch is describable by a simple function of $R_{\odot}(t)/R_{\odot}(\text{today})$.

We limit the time period covered in Figure 4 and Figure 5 to be less than 6.5 billion years, since between 6.5 and 7.0 billion years of age semi-convection begins to influence noticeably the computed quantities characterizing the convective zone. The physics required to calculate accurately the influence of semi-convection is beyond the range of the present paper.

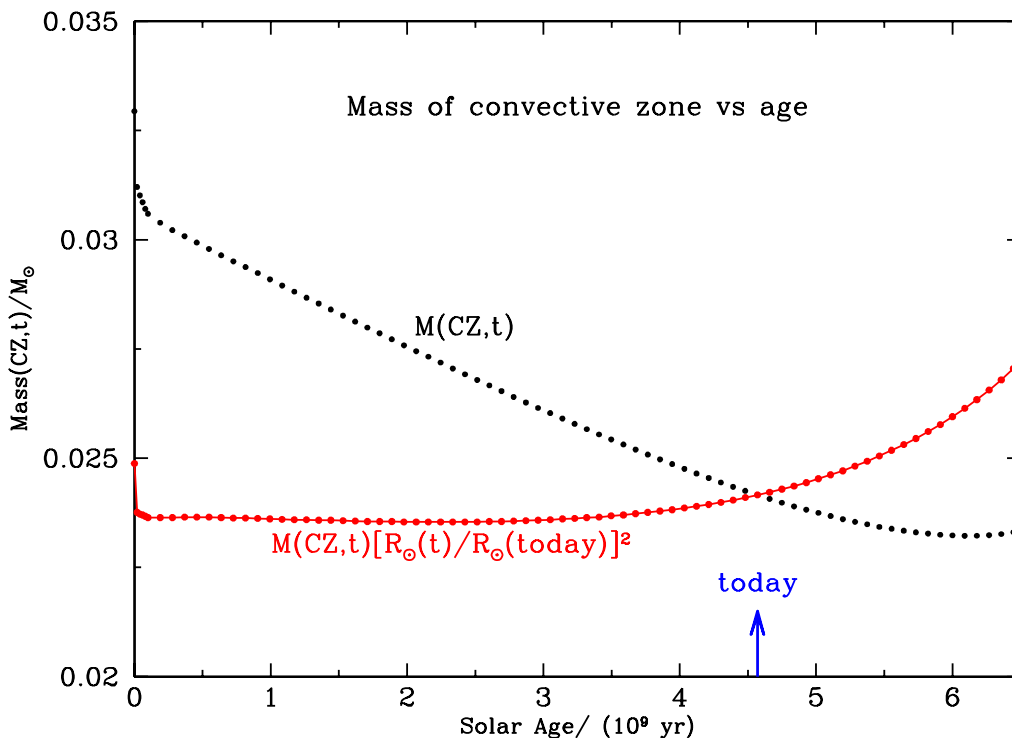


Fig. 5.— The mass included within the convective zone, $M(\text{CZ}, t)$, as a function of age for the standard solar model. The mass of the convective zone is measured in units of $M_{\odot}(\text{today})$ and the solar age is measured in units of 10^9 yr. The mass of the convective zone is approximately proportional to $R_{\odot}(t)^{-2}$.

From the zero age main sequence to the present solar age, the depth of the convective zone is approximately proportional to the contemporary solar radius, $R_{\odot}(t)$, i.e.,

$$0.714 \leq R(\text{CZ}, t)/R_{\odot}(t) \leq 0.722. \quad (2)$$

The zero-age main sequence value is $R(\text{CZ}, t = 0) = 0.627R_{\odot}(\text{today})$ and the present-day value is $R(\text{CZ}, \text{today}) = 0.714R_{\odot}(\text{today})$, which corresponds to an approximately 14% decrease in the depth of the convective zone over the age of the sun. However, if we normalize the depth of the convective zone to the contemporary solar radius, the change is very small, $R(\text{CZ}, t = 0) = 0.722R_{\odot}(t = 0)$ and $R(\text{CZ}, \text{today}) = 0.714R_{\odot}(\text{today})$. After 6.5 billion years, $R(\text{CZ}, t = 6.5) = 0.764R_{\odot}(\text{today})$ and, in terms of the contemporary solar radius, $R(\text{CZ}, t = 6.5) = 0.706R_{\odot}(t = 6.5)$. The relative evolution between the convective zone depth and the total solar radius, $d[R(\text{CZ}, t)/R_{\odot}(t)]/dt = -0.002$ per 10^9 yr, is very slow.

Over the period from the initial age main sequence to the present epoch, the mass of the solar convective zone decreases with time as $R_{\odot}(t)^{-2}$,

$$M(\text{CZ}, t) \times R_{\odot}(t)^2 = \text{constant} \quad (3)$$

to an accuracy of about $\pm 1\%$. The zero-age main sequence value of the mass included within the convective zone is $0.0329M_{\odot}$, which decreases to $0.02415M_{\odot}$ at the present epoch. However, this proportionality is no longer valid for larger ages, as can be seen in Figure 5. The mass of the convective zone is $M(\text{CZ}, 6.5) = 0.0233M_{\odot}$ at 6.5 billion years. At about 6.8 billion years, the previous monotonic decrease of the mass of the convective zone is reversed and $M(\text{CZ}, t)$ begins to increase with time. This behavior is not shown in Figure 5 since the calculated increase in the mass of the convective zone occurs in the same time frame as the onset of semi-convection.

Figure 6 shows some properties at the base of the convective zone as a function of solar age. The figure displays the time dependence of the temperature, $T(\text{CZ}, t)$ (solid curve),

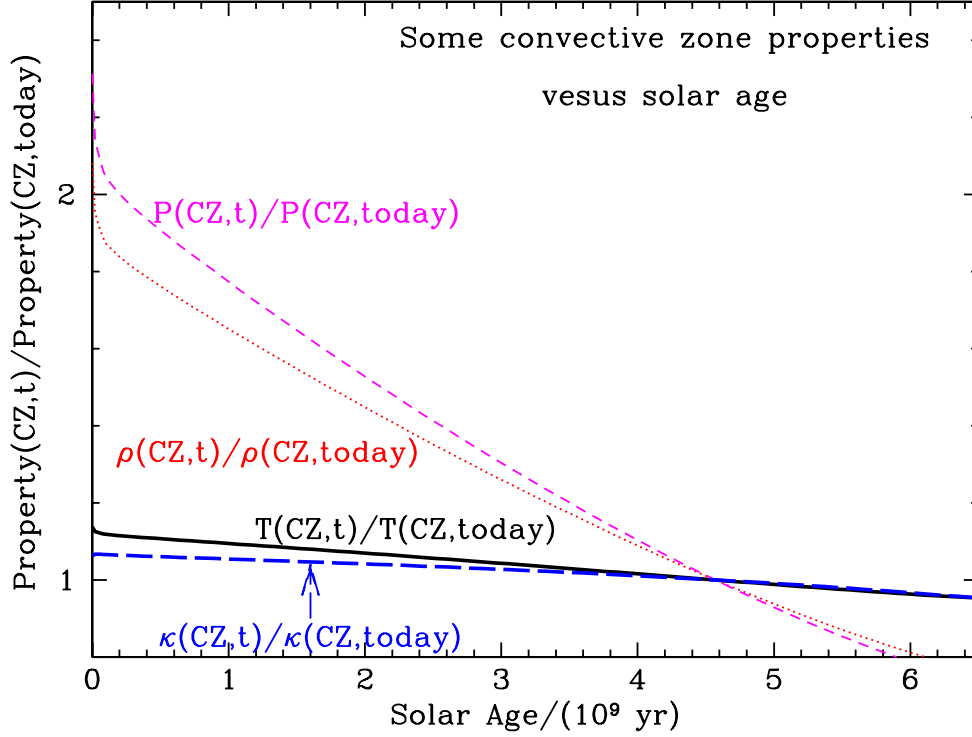


Fig. 6.— Some properties at the base of the convective zone as a function of age for the Standard solar model. The properties shown are the temperature, $T(\text{CZ},t)$ (solid curve), the density, $\rho(\text{CZ},t)$ (dotted), the pressure, $P(\text{CZ},t)$ (short dashes), and the radiative opacity, $\kappa(\text{CZ},t)$ (long dashes). All of the quantities are normalized by dividing by their values at the present epoch. After 6.5 billion yr, semi-convection begins to be important.

the density, $\rho(\text{CZ},t)$ (dotted), the pressure, $P(\text{CZ},t)$ (short dashes), and the radiative opacity, $\kappa(\text{CZ},t)$ (long dashes). For convenience in plotting, each of the physical variables has been divided by its value at the current epoch. In cgs units, the Standard model parameters have the following values at an age of 4.57×10^9 yr: $T(\text{CZ}, \text{today}) = 2.18 \times 10^6$ K, $\rho(\text{CZ}, \text{today}) = 0.19$, $P(\text{CZ}, \text{today}) = 5.58 \times 10^{13}$, and $\kappa(\text{CZ}, \text{today}) = 20.5$.

The temperature at the base of the convective zone decreases by 14% from the zero-age main-sequence to the current solar age, i. e., to a good approximation

$$T(\text{CZ}, t) \propto R(\text{CZ}, t)^{-1}. \quad (4)$$

The opacity at the base of the convective zone decreases by 6% over the same period. The density and the pressure at the base of the convective zone decrease by much larger quantities, by factors of 2.1 and 2.3, respectively. Equation 4 is valid to an accuracy of about $\pm 1\%$ throughout the 6.5×10^9 yr shown in Figure 6.

The base of the convective zone is defined by the Schwarzschild criterion. Because the adiabatic gradient is nearly constant in time, the equations of stellar structure imply that the quantity $\kappa PL/MT^4$ will be approximately constant at the base of the convective zone. From Figure 6, we see that both the opacity and the temperature decrease slowly at the base of the convective zone. Solar models therefore compensate for the increase of the luminosity by the decrease of the pressure at the boundary between radiative and convective equilibrium.

3.4. Central values of Temperature, Density, and Pressure

Figure 7 shows the time dependence of the central values for the temperature, density, and pressure of the Standard solar model. The results are normalized to the computed values for the present epoch.

Over the 8 billion years shown in Figure 7, the central temperature increases by about 39%. At the zero-age main sequence, the central temperature is 13.5×10^9 K and is 15.7×10^9 K at the current epoch; the central temperature of the model reaches 18.8×10^9 K at a solar age of 8 billion years. This increase is very similar to that of the solar radius. In fact, the central value of the temperature is, to a reasonable approximation, proportional to the solar radius, $R_\odot(t)$. The ratio

$$T_c(t)/R_\odot(t) = \text{constant} \tag{5}$$

to an accuracy of $\pm 1.5\%$ ($\pm 3\%$) from the zero ago-main sequence to the current epoch (to

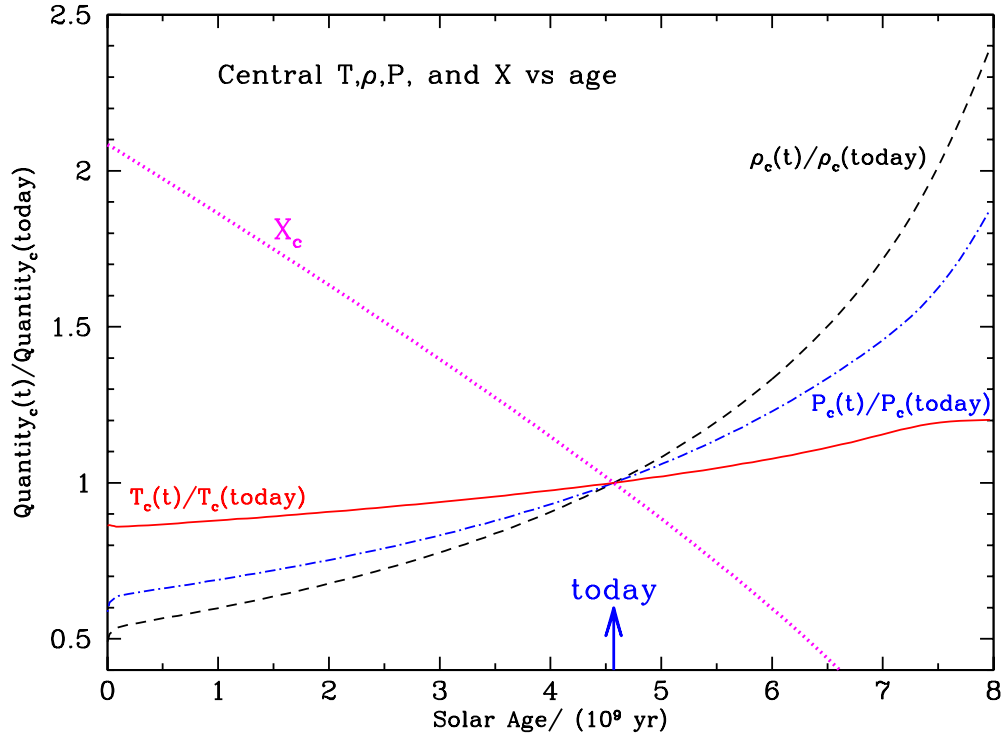


Fig. 7.— The temporal evolution of the central temperature, density, pressure, and hydrogen mass fraction. The figure shows the computed values for the Standard solar model of the central temperature (solid line), pressure (dot-dash line), density (dash line), and hydrogen mass fraction (dotted line).

a solar age of 6.5 billion years).

The sun derives its luminosity by burning hydrogen into helium. The hydrogen mass fraction at the center of the sun, X_c , decreases from 0.708 at the zero-age main sequence to 0.340 at the current epoch, a decrease by more than a factor of two. At an of 6.5 billion years, the mass fraction has decreased to 0.145, a decrease by a factor of almost five from the zero-age value. The remaining hydrogen is burned very quickly, with X_c reaching 0.008 at a solar age of 8 billion years.

The pressure is inversely proportional to the mean molecular weight and is also proportional to the temperature and to the density. As the sun burns hydrogen into helium,

the mean molecular weight in the center of the solar model increases from about 0.6 in the initial sun to about 1.2 in the current-age solar model. Thus the increase with time of the temperature and density is partially cancelled, in computing the pressure, by the increase with time of the mean molecular weight.

4. Variant and deviant solar models

In this section, we describe eleven solar models, seven of which are slight variants on the theme of the standard solar model (see § 4.1) and four of which are deficient in one or more significant aspects of the physics used in their construction (see § 4.2). Nine of these solar models have been described in detail in BPB2000, where their helioseismological properties were investigated extensively. Hence the descriptions here will be brief.

Table 4 and Table 5 summarize some of the important physical characteristics of the complete set of the nine solar models whose helioseismological properties we studied in BPB2000 plus two models with slightly lower values of Z/X that are studied here for the first time. We present in Table 4 for each of the models the central temperature, density, and pressure; the helium and heavy element mass fractions in the initial model; the helium and heavy element mass fractions in the solar center. We give in Table 5 the helium and heavy element abundances at the solar surface; the mixing length parameter, α ; and the radius and temperature at the base of the convective zone, as well as the mass included in the convective zone. All quantities are shown for the model at the present epoch.

We will now define the eleven Variant and Deviant solar models.

Table 4: Some interior characteristics of the solar models. The quantities T_c (in units of 10^7 K), ρ_c (10^2 gm cm $^{-3}$), and P_c (10^{17} erg cm $^{-3}$) are the current epoch central temperature, density, and pressure; Y and Z are the helium and heavy element mass fractions, where the subscript ‘init’ denotes the zero-age main sequence model, and the subscript ‘c’ denotes the center of the solar model.

Model	T_c	ρ_c	P_c	Y_{init}	Z_{init}	Y_c	Z_c
Standard	15.696	152.7	2.342	0.2735	0.0188	0.6405	0.0198
NACRE	15.665	151.9	2.325	0.2739	0.0188	0.6341	0.0197
AS00	15.619	152.2	2.340	0.2679	0.0187	0.6341	0.0197
GN93	15.729	152.9	2.342	0.2748	0.02004	0.6425	0.02110
Pre-M.S.	15.725	152.7	2.339	0.2752	0.02003	0.6420	0.02109
Rotation	15.652	148.1	2.313	0.2723	0.01934	0.6199	0.02032
Radius ₇₈	15.729	152.9	2.342	0.2748	0.02004	0.6425	0.02110
Radius ₅₀₈	15.728	152.9	2.341	0.2748	0.02004	0.6425	0.02110
No Diffusion	15.448	148.6	2.304	0.2656	0.01757	0.6172	0.01757
Old physics	15.787	154.8	2.378	0.2779	0.01996	0.6439	0.02102
$S_{34} = 0$	15.621	153.5	2.417	0.2722	0.02012	0.6097	0.02116
Mixed	15.189	90.68	1.728	0.2898	0.02012	0.3687	0.02047

4.1. Variant solar models

The NACRE model was constructed using the same input physics as our Standard model except that we use for the NACRE model the charged particle fusion cross sections recommended in the NACRE compilation (Angulo et al. 1999). We specify the fusion cross used for this model more fully in § 5.1.3. The model GN93 was considered our Standard model in BPB2000 and differs only in the adopted value of $Z/X = 0.0245$ (Grevesse & Noels 1993) from the current Standard model (see § 2) which has $Z/X = 0.0230$ (Grevesse & Sauval 1998). The model AS00 is the same as the two models described above except that

Table 5: Some characteristics of the convective zones of solar models at the current epoch. Here Y_s and Z_s are the surface helium and heavy element abundances, α is the mixing length parameter, $R(\text{CZ})$ and $T(\text{CZ})$ are the radius and temperature at the base of the convective zone, and $M(\text{CZ})$ is the mass included within the convective zone.

Model	Y_s	Z_s	α	$R(\text{CZ})$ (R_\odot)	$M(\text{CZ})$ (M_\odot)	$T(\text{CZ})$ (10^6 K)
Standard	0.2437	0.01694	2.04	0.7140	0.02415	2.18
NACRE	0.2443	0.01696	2.04	0.7133	0.02451	2.19
AS00	0.2386	0.01684	2.05	0.7141	0.02394	2.18
GN93	0.2450	0.01805	2.06	0.7124	0.02457	2.20
Pre-M.S.	0.2455	0.01805	2.05	0.7127	0.02443	2.20
Rotation	0.2483	0.01797	2.03	0.7144	0.02388	2.15
Radius ₇₈	0.2450	0.01806	2.06	0.7123	0.02461	2.20
Radius ₅₀₈	0.2450	0.01806	2.06	0.7122	0.02467	2.20
No Diffusion	0.2655	0.01757	1.90	0.7261	0.02037	2.09
Old physics	0.2476	0.01796	2.04	0.7115	0.02455	2.21
$S_{34} = 0$	0.2422	0.01811	2.03	0.7151	0.02309	2.17
Mixed	0.2535	0.01782	1.85	0.7315	0.01757	2.02

it has lower heavy element abundance $Z/X = 0.0226$ (Asplund 2000). As a consequence of a more detailed calculation of the solar atmosphere, Asplund (2000) suggests that all meteoritic abundances should be adjusted downward by 0.04 dex. All of the models described below, in § 4.2 as well as in this subsection, use the Grevesse and Noels (1993) composition mix with $Z/X = 0.0245$.

Model Pre-M.S. is evolved from the pre-main sequence stage, but otherwise is the same as our Standard model. The model Rotation incorporates mixing induced by rotation and is a reasonable upper bound to the degree of rotational mixing which is consistent with the

observed depletion of lithium in the sun ³(Pinsonneault et al. 1999). The prescriptions for calculating this model are described in Section 5 of Pinsonneault (1997) and in BPB2000. There has been considerable discussion recently regarding the precise value of the solar radius (cf. Antia 1998; Schou et al. 1997; Brown & Christensen-Dalsgaard 1998) and some discussion of the effects of the uncertainty in radius on the quantities inferred from the helioseismological inversions (cf. Basu 1998). We have therefore considered two models which were constructed with the same input physics as BP2000, but which have model radii which differ from the radius assumed in constructing the Standard model. Radius₇₈ has a radius of 695.78 Mm, which is the radius that has been determined from the frequencies of f-modes (cf. Antia 1998) and Radius₅₀₈ has a radius of 695.508 Mm, which is the solar radius as determined by Brown & Christensen-Dalsgaard (1998), who used the measured duration of solar meridian transits during the 6 years 1981–1987 and combined these measurements with models of the solar limb-darkening function to estimate the value of the solar radius.

All of these variant models are approximately as consistent with the helioseismological evidence as the Standard model (see BPB2000). For example, the rms sound speed differences between the variant models and BP2000 are: 0.03% (Pre-M.S.), 0.08% (Rotation), 0.15% (Radius₇₈), and 0.03% (Radius₅₀₈). The average difference (rms) between the four variant models and the Standard model is 0.07% . We shall see in § 5 that the differences predicted by these models for the important neutrino fluxes are all less than 5%.

³The Rotation model discussed here differs somewhat from the rotation model analyzed in BPB2000 in that the metals heavier than CNO were inadvertently not mixed in the previous version of this model.

4.2. Deviant solar models

The model ‘Old physics’ was constructed using the old Yale equation of state (cf. Guenther et al. 1992), supplemented with the Debye-Hückel correction (cf. Bahcall, Bahcall, & Shaviv 1968) and older OPAL radiative opacities (Iglesias, Rogers, & Wilson 1992; Kurucz 1991). The model includes helium and heavy element diffusion and nuclear reaction cross section data in the same way as our Standard model. The $S_{34} = 0$ model was calculated assuming that the rate of the ${}^3\text{He}(\alpha, \gamma){}^7\text{Be}$ reaction is zero, which implies that no ${}^7\text{Be}$ or ${}^8\text{B}$ neutrinos are produced. In the Standard solar model, about 12% of the terminations of the $p - p$ chain involve the ${}^3\text{He}(\alpha, \gamma){}^7\text{Be}$ reaction, whose rate is proportional to S_{34} . The No Diffusion model does not include helium or heavy-element diffusion and therefore represents the state-of-the art in solar modeling prior to 1992 (cf. Bahcall & Ulrich 1988; Bahcall & Pinsonneault 1992; Proffitt 1994). The model Mixed has an artificially mixed core, with the inner 50% by mass (25% by radius) required to be chemically homogeneous at all times. This model was constructed to be similar to the prescription of Cumming & Haxton (1996), who changed by hand the ${}^3\text{He}$ abundance as a function of radius in the final BP95 (Bahcall & Pinsonneault 1995) solar model in order to minimize the discrepancy between measurements of the total event rates in neutrino experiments and the calculated event rates. Cumming and Haxton did not calculate the time evolution of their model.

We showed in BPB2000 that the Mixed, No Diffusion, and $S_{34} = 0$ models are strongly disfavored by helioseismological data. We use these deviant (or deficient) models here to test the robustness of the discrepancies between solar model predictions and solar neutrino measurements. We have already seen in Figure 2 that the luminosity evolution predicted by solar models is essentially the same for the deviant models and for the Standard solar model.

5. Neutrino Physics

This section presents neutrino fluxes and predicted event rates in different solar neutrino experiments; the fluxes and event rates are calculated using the eleven solar models described in § 4. We also give other aspects of the solar model that influence the interpretation of solar neutrino experiments.

As described in § 2.2, we present at <http://www.sns.ias.edu/~jnb> a detailed numerical table which gives the fraction of each of the eight important neutrino fluxes that is produced in each spherical shell. These neutrino production fractions are important for calculating the effect of MSW (matter) oscillations in the sun, but will not be discussed further here.

Section 5.1 presents the fluxes of electron type neutrinos that are produced in the sun according to the Standard solar model and to the eight variant solar models considered in this paper. We compare the results of these predictions with measurements of the total rates in the chlorine solar neutrino experiment, the SAGE and GALLEX + GNO gallium experiments, and the Kamiokande and SuperKamiokande water Cherenkov detectors. We also describe in this section how we estimate the errors (asymmetric in some cases) on the predicted fluxes and event rates.

In § 5.2, we present detailed results for the electron number density versus solar radius. The MSW conversion of electron type neutrinos to other neutrino types depends upon the radial distribution of the electron number density. In previous presentations of the Standard model, we have not given the electron number density in the outer parts of the sun with sufficient precision to permit calculations of a subset of the currently allowed matter transitions. Section 5.3 presents the calculated time-dependences of the most important solar neutrino fluxes, the pp , ${}^7\text{Be}$, ${}^8\text{B}$, and ${}^{13}\text{N}$ neutrino fluxes.

5.1. Neutrino fluxes and experimental event rates at the current epoch

We present in § 5.1.1 the neutrino fluxes and experimental event rates predicted by the Standard model and contrast these results with the observed rates. In § 5.1.2, we describe the procedures and the ingredients used to calculate the uncertainties in the neutrino fluxes and the event rates. We compare in § 5.1.4 the calculated neutrino fluxes and experimental event rates for the eight variant and deviant solar models with the results for the Standard model and with the measured solar neutrino event rates.

5.1.1. Standard model

Table 6 gives the neutrino fluxes and their uncertainties for our Standard solar model. The adopted uncertainties in different input parameters are given in Table 2 of Bahcall, Basu, & Pinsonneault (1998), which we refer to hereafter as BP98. We also present in Table 6 the calculated event rates in the chlorine, gallium, and lithium experiments. The rate in the Super-Kamiokande experiment is usually quoted as a fraction of the best-estimate theoretical flux of ^8B neutrinos, assuming an undistorted (standard) energy spectrum.

Table 7 compares the predictions of the combined standard model, i. e., the standard solar model (BP2000) and the standard electroweak theory (no neutrino oscillations), with the results of the chlorine, GALLEX + GNO, SAGE, Kamiokande, and Super-Kamiokande solar neutrino experiments. The observed rate in the chlorine experiment is 2.56 ± 0.23 SNU (Lande 2000; Davis 1994; Cleveland et al. 1998), which is to be compared to the calculated value of $7.7^{+1.3}_{-1.1}$ SNU. This discrepancy between calculated and observed neutrino capture rates has been approximately the same for more than three decades (cf. Bahcall, Bahcall, & Shaviv 1968; Davis, Harmer, & Hoffman 1968; Bahcall 1989).

The average of the SAGE (Abdurashitov et al. 1999; Gavrin 2000) and the GALLEX

Table 6: Standard Model Predictions (BP2000): solar neutrino fluxes and neutrino capture rates, with 1σ uncertainties from all sources (combined quadratically). The observed capture rates are: 2.56 ± 0.23 SNU [chlorine (Lande 2000)] and 74.7 ± 5.0 SNU [combined SAGE and GALLEX plus GNO (Hampel et al. 1999; Abdurashitov et al. 1999; Belotti 2000)]. The ${}^8\text{B}$ flux measured by the Super-Kamiokande experiment is $2.40 \pm 0.03(\text{stat})_{-0.07}^{+0.08}(\text{syst.}) \text{ cm}^{-2}\text{s}^{-1}$ (Suzuki 2000).

Source	Flux ($10^{10} \text{ cm}^{-2}\text{s}^{-1}$)	Cl (SNU)	Ga (SNU)	Li (SNU)
pp	$5.96 (1.00_{-0.01}^{+0.01})$	0.0	69.9	0.0
pep	$1.40 \times 10^{-2} (1.00_{-0.015}^{+0.015})$	0.22	2.9	9.2
hep	9.3×10^{-7}	0.04	0.1	0.1
${}^7\text{Be}$	$4.82 \times 10^{-1} (1.00_{-0.10}^{+0.10})$	1.16	34.5	9.2
${}^8\text{B}$	$5.15 \times 10^{-4} (1.00_{-0.16}^{+0.20})$	5.87	12.3	20.1
${}^{13}\text{N}$	$5.56 \times 10^{-2} (1.00_{-0.17}^{+0.21})$	0.09	3.4	2.4
${}^{15}\text{O}$	$4.88 \times 10^{-2} (1.00_{-0.19}^{+0.25})$	0.33	5.5	12.0
${}^{17}\text{F}$	$5.73 \times 10^{-4} (1.00_{-0.25}^{+0.25})$	0.0	0.1	0.1
Total		$7.7_{-1.1}^{+1.3}$	129_{-7}^{+9}	$53.0_{-6.1}^{+6.6}$

Note. — The cross sections for neutrino absorption on chlorine are from Bahcall et al. (1996); the cross sections for gallium are from Bahcall (1997); the cross sections for ${}^7\text{Li}$ are from Bahcall (1989) and Bahcall (1994).

(Hampel et al. 1999) plus GNO (Belotti 2000) results is 74.7 ± 5.0 SNU, which is more than 6σ away from the calculated standard rate of 129_{-7}^{+9} SNU.

After 1117 days of data acquisition, the flux of ${}^8\text{B}$ neutrinos measured by Super-Kamiokande is $2.40 \pm 0.03(\text{stat})_{-0.07}^{+0.08}(\text{syst.}) \text{ cm}^{-2}\text{s}^{-1}$ (Suzuki 2000; Fukuda et al. 1998), which corresponds to 0.466 of the BP2000 predicted flux.

Comparing the second and third columns of Table 7, we see that the predictions of the

Table 7: Solar Neutrino Rates: Theory versus Experiment. The units are SNO (10^{-36} interactions per atom per sec) for the radiochemical experiments: Chlorine, GALLEX + GNO, and SAGE. The unit for the ^8B and hep fluxes are, respectively, $10^6 \text{ cm}^{-2} \text{ s}^{-1}$ and $10^3 \text{ cm}^{-2} \text{ s}^{-1}$. The errors quoted for Measured/BP2000 are the quadratically combined uncertainties for both BP2000 and the Measured rates. For simplicity in presentation, asymmetric errors were averaged. References to the experimental results are given in the text and in Lande (2000), Belotti (2000), Gavrin (2000), Fukuda et al. (1996), and Suzuki (2000) for the chlorine, GALLEX + GNO, SAGE, Kamiokande, and Super-Kamiokande results.

Experiment	BP2000	Measured	Measured/BP2000
Chlorine	$7.7_{-1.1}^{+1.3}$	2.56 ± 0.23	0.33 ± 0.06
GALLEX + GNO	129_{-7}^{+9}	$74.1_{-7.8}^{+6.7}$	0.57 ± 0.07
SAGE	129_{-7}^{+9}	$75.4_{-7.4}^{+7.8}$	0.58 ± 0.07
^8B -Kamiokande	$5.15 [1.00_{-0.16}^{+0.20}]$	$2.80 [1.00 \pm 0.14]$	0.54 ± 0.13
^8B -Super-Kamiokande	$5.15 [1.00_{-0.16}^{+0.20}]$	$2.40 [1.00_{-0.03}^{+0.04}]$	0.47 ± 0.09
hep-Super-Kamiokande	9.3	$11.3(1 \pm 0.8)$	~ 1

combined standard model differ by many standard deviations from the results of the solar neutrino experiments.

The flux of *hep* neutrinos was calculated for BP2000 using the most recent theoretical evaluation by Marcucci et al. (2000) of the cross section factor $S_0(\text{hep})$, which is 4.4 times larger than the previous best estimate. The most recent preliminary report (after 1117 days of data) of the SuperKamiokande collaboration (Suzuki 2000) is that the *hep* flux observed in their $\nu_e - e$ scattering experiment is 5.4 ± 4.5 times the best-estimate from BP98. Since the BP2000 estimate of the *hep* flux is a factor of 4.4 times larger than the flux quoted in BP98, the best-estimate theoretical *hep* flux now agrees with the best-estimate experimental *hep* flux measurement, although we do not attach much significance to this agreement since we cannot quote an uncertainty on the theoretical estimate (see discussion of the *hep* reaction in § 5.1.2).

The event rates predicted by BP2000 for the chlorine, gallium, and SuperKamiokande

solar neutrino experiments are the same, to the accuracy indicated in Table 6, as the rates predicted for the BP98 standard solar models. As far as these experiments are concerned, the effects of using the improved heavy element composition cancels the effect of correcting the error the opacity interpolation (see Section 2.1). The difference in the ${}^7\text{Be}$ flux predicted by BP98 and BP2000 is only 0.4%. The ${}^7\text{Be}$ flux will be measured by the BOREXINO solar neutrino experiment.

5.1.2. *Calculated uncertainties*

We have calculated the uncertainties in the neutrino fluxes and in the experimental event rates by including the published errors in all experimental quantities and by taking account of the correlated influence of different input parameters using the results of detailed solar model calculations. The procedure for calculating the uncertainties has been developed over the past three decades and is described in detail in Chapter 7 of Bahcall (1989) (see also Bahcall & Pinsonneault 1992, 1995, and Bahcall, Basu, & Pinsonneault 1998).

In order that the reader can see the specific implementation of the uncertainty calculations, we are making available the exportable fortran code that evaluates the rates in different neutrino experiments and also calculates the uncertainties in the individual neutrino fluxes and experimental rates. The code, `exporates.f`, is available at <http://www.sns.ias.edu/~jnb/SNdata/sndata.html> .

The uncertainties in the nuclear fusion cross sections (except for *hep*, see below) were taken from Adelberger et al. (1998), the neutrino cross section uncertainties from Bahcall (1994, 1996, 1997), the heavy element uncertainty was taken from helioseismological measurements, Basu & Antia (1997), the luminosity and age uncertainties were adopted from Bahcall & Pinsonneault (1995), the 1σ fractional uncertainty in the diffusion rate was

taken to be 15% (Thoul, Bahcall, & Loeb 1994) and the opacity uncertainty was determined by comparing the results of fluxes computed using the older Los Alamos opacities with fluxes computed using the modern Livermore opacities (Bahcall & Pinsonneault 1992).

We follow the discussion in Bahcall & Pinsonneault (1995) and adopt a 1σ uncertainty in the heavy element abundance of

$$\sigma(Z/X) = \pm 0.061 \times (Z/X). \quad (6)$$

This uncertainty spans the range of values recommended by Grevesse (1984), Grevesse & Noels (1993), and Grevesse & Sauval (1998) over the fourteen year period covered by the cited Grevesse et al. review articles. The uncertainty adopted here is about twice as large as the uncertainty recommended by Basu & Antia (1997) based on their helioseismological analysis. In support of the larger uncertainty used in this paper, we note that the difference between the Grevesse & Noels (1993) values of $Z/X = 0.0230$ is 1σ according to Eq. (6).

We include for the first time in this series of papers the uncertainty in the small ^{17}F neutrino flux due to the uncertainty in the measured S_0 -factor for the reaction $^{16}\text{O}(p, \gamma)^{17}\text{F}$. We use the 1σ uncertainty 18.1% estimated by Adelberger et al. (1998). It was an oversight not to include this uncertainty in our previous calculations.

The only flux for which we do not quote an estimated uncertainty is the *hep* flux (see Table 6). The difficulty of calculating from first principles the nuclear cross section factor $S_0(\text{hep})$ is what has caused us not to quote in this series of papers an uncertainty in the *hep* flux (see discussion in Bahcall 1989 and in Bahcall and Krastev 1998). The *hep* reaction is uniquely difficult to calculate among the light element fusion reactions since the one-body and two-body contributions to the reaction rate are comparable in magnitude but opposite in sign, so that the net result is sensitive to a delicate cancellation. Also, two-body axial currents from excitations of Δ isobars are model dependent. In addition, the calculated rate is sensitive to small components in the wave function, particularly *D*-state admixtures

generated by tensor interactions. These complications have been discussed most recently and most thoroughly by Marcucci et al. (2000b).

The calculated errors are asymmetric in many cases. These asymmetries in the uncertainties in the neutrino fluxes and experimental event rates result from asymmetries in the uncertainties of some of the input parameters, for example, the important pp , ${}^7\text{Be} + p$, and ${}^{14}\text{N} + p$ fusion reactions and the effect of excited states on neutrino absorption cross sections. To include the effects of asymmetric errors, the code `exportrates.f` was run with different input representative uncertainties and the different higher (lower) rates were averaged to obtain the quoted upper (lower) limit uncertainties.

5.1.3. *NACRE charged particle fusion rates*

In order to estimate the systematic uncertainties associated with different treatments of the nuclear fusion reactions, we have constructed a solar model that is the same as the Standard Model discussed in Section 5.1.1, except that we have used the charged particle fusion cross sections recommended in the NACRE compilation (Angulo et al. 1999) rather than the fusion cross sections determined by Adelberger et al. (1998). We will refer to this solar model as the NACRE model.

The low energy cross section factors, S_0 , that are recommended by the NACRE collaboration and by Adelberger et al. agree within their stated 1σ uncertainties for all of the fusion reactions that are important for constructing a solar model. The only important solar nuclear reactions for which the NACRE collaboration did not recommend interaction rates are the electron capture reactions that produce the ${}^7\text{Be}$ and the pep neutrinos; the NACRE collaboration also did not provide energy derivatives for the cross section factors of the CNO reactions. Wherever the data necessary for computing solar fusion rates was

Table 8: Neutrinos with NACRE reaction rates. The solar neutrino fluxes and neutrino capture rates that were calculated with the NACRE fusion cross sections (Angulo et al. 1999) are given in the table. The only difference between the model used in this calculation and the Standard Model, whose fluxes are given in Table 6, is that the Adelberger et al. (1998) fusion cross sections were replaced by the NACRE cross sections for all reactions for which the NACRE collaboration quoted zero-energy cross section factors, S_0 .

Source	Flux ($10^{10} \text{ cm}^{-2}\text{s}^{-1}$)	Cl (SNU)	Ga (SNU)	Li (SNU)
pp	$5.97 (1.00^{+0.01}_{-0.01})$	0.0	70.0	0.0
pep	$1.39 \times 10^{-2} (1.00^{+0.015}_{-0.015})$	0.22	2.8	9.1
hep	9.4×10^{-7}	0.04	0.1	0.1
^7Be	$4.85 \times 10^{-1} (1.00^{+0.10}_{-0.10})$	1.16	34.8	9.2
^8B	$5.54 \times 10^{-4} (1.00^{+0.20}_{-0.16})$	6.32	13.3	21.6
^{13}N	$4.93 \times 10^{-2} (1.00^{+0.21}_{-0.17})$	0.08	3.0	2.1
^{15}O	$4.24 \times 10^{-2} (1.00^{+0.25}_{-0.19})$	0.29	4.8	10.4
^{17}F	$5.39 \times 10^{-4} (1.00^{+0.25}_{-0.25})$	0.0	0.1	0.1
Total		$8.1^{+1.4}_{-1.1}$	129^{+9}_{-7}	$52.7^{+6.6}_{-6.0}$

Note. — The cross sections for neutrino absorption on chlorine are from Bahcall et al. (1996); the cross sections for gallium are from Bahcall (1997); the cross sections for ^7Li are from Bahcall (1989) and Bahcall (1994).

not available in the NACRE compilation, we continued to use the Adelberger et al. (1998) recommended values in computing the NACRE model.

Table 8 gives the calculated neutrino fluxes and capture rates predicted by the NACRE solar model. In all cases, the fluxes for the NACRE solar model agree with the fluxes calculated with the Standard solar model to well within the 1σ uncertainties in the Standard Model fluxes. The ^7Be flux from the NACRE model is 1% larger than for the Standard

model and the ^8B flux is 8% higher. The chlorine capture rate predicted by the NACRE model is 5% higher than for the Standard model; the predicted rates for the NACRE model and the Standard model differ by less than 1% for the gallium and lithium experiments.

We conclude that this estimate of the systematic uncertainties due to the relative weights given to different determinations of nuclear fusion cross sections suggests likely errors from this source that are significantly smaller than our quoted 1σ errors for the Standard model neutrino fluxes and event rates (cf. Table 6).

5.1.4. Variant and deviant models

Table 9 compares the calculated neutrino fluxes for the seven variant solar models described in § 4.1 and for the four deficient solar models described in § 4.2 with the fluxes obtained for the Standard solar model. The range of the ^8B neutrino fluxes among the seven standard-like models (rows 1–7 of Table 9) is only $\pm 7\%$, a factor of two or three smaller than the uncertainty (due to other sources) in the calculated ^8B flux of the Standard model (see Table 6). The spread in ^7Be flux is $\pm 3\%$; the range in ^{37}Cl and ^{71}Ga rates is ± 0.45 SNU and ± 2 SNU, respectively.

The deviant models listed in Table 9 are all deficient in some important aspect of the physics used in their calculation. The No Diffusion, Old Physics, $S_{34} = 0$, and Mixed models all give such bad agreement with helioseismology (compared to the first seven models) that the comparison with the data cannot be made on the same scale as for the standard-like models (see BPB2000). The Old Physics model gives a rms difference between the calculated and measured sound speeds that is more than twice as large as when the Standard model is used. For the $S_{34} = 0$ model, the rms discrepancy is seven times worse in the solar interior than for the standard model; for the No Diffusion model, the disagreement

Table 9: Neutrino fluxes from twelve solar models. The table lists the calculated neutrino fluxes and event rates for the seven variant solar models that are discussed in § 4.1 and for the four deficient solar models that are discussed in § 4.2, and compares the results with the Standard model fluxes. The models in rows two through eight are all variants on the Standard model (first row). The last four models are deficient in some important aspect of the physics used in their construction and do not provide good fits to the helioseismological data.

Model	pp	pep	hep	${}^7\text{Be}$	${}^8\text{B}$	${}^{13}\text{N}$	${}^{15}\text{O}$	${}^{17}\text{F}$	Cl	Ga
	(E10)	(E8)	(E3)	(E9)	(E6)	(E8)	(E8)	(E6)	(SNU)	(SNU)
Standard	5.96	1.40	9.3	4.82	5.15	5.56	4.88	5.73	7.7	129
NACRE	5.97	1.39	9.4	4.85	5.54	4.93	4.24	5.39	8.1	129
AS00	5.99	1.41	9.4	4.62	4.70	5.25	4.56	5.33	7.1	126
GN 93	5.94	1.39	9.2	4.88	5.31	6.18	5.45	6.50	8.0	130
Pre-M.S.	5.95	1.39	9.2	4.87	5.29	6.16	5.43	6.47	7.9	130
Rotation	5.98	1.40	9.2	4.68	4.91	5.57	4.87	5.79	7.4	127
Radius ₇₈	5.94	1.39	9.2	4.88	5.31	6.18	5.45	6.50	8.0	130
Radius ₅₀₈	5.94	1.39	9.2	4.88	5.31	6.18	5.45	6.50	8.0	130
No Diffusion	6.05	1.43	9.6	4.21	3.87	4.09	3.46	4.05	6.0	120
Old physics	5.95	1.41	9.2	4.91	5.15	5.77	5.03	5.92	7.8	130
$S_{34} = 0$	6.40	1.55	10.1	0.00	0.00	6.47	5.64	6.70	0.8	89
Mixed	6.13	1.27	6.2	3.57	4.13	3.04	3.05	3.61	6.1	115

is about seven times worse averaged over the sun than for the standard model. The Mixed model is the worst of all; the rms disagreement in the solar core is about 25 times larger than for the standard solar model.

Even if one is willing to consider solar models that predict sound speeds which deviate so drastically from the measured helioseismological values, the four deviant solar models do not describe well the solar neutrino data. For the Old Physics, No Diffusion, and Mixed solar models, the predicted rates for the gallium experiments lie between 115 SNU and 130

SNU, which is to be contrasted with the observed rate of 75 ± 5 SNU, which is at least an 8σ discrepancy. For the $S_{34} = 0$ model, the predicted rate in the chlorine experiment is 0.79 SNU, which is also about eight standard deviations less than the observed value, 2.56 ± 0.23 SNU.

5.2. The electron number density

The probability of converting an electron type neutrino to a muon or tau neutrino in the Sun depends upon the profile of the electron number density as a function of solar radius. For particular values of the electron density, neutrino energy, and neutrino mass, neutrinos can be resonantly converted from one type of neutrino to another. The Mikheyev-Smirnov resonance occurs if the electron density at a radius r satisfies

$$\frac{n_{e,res}(r)}{N_A} \approx 66 \cos 2\theta_V \left(\frac{|\Delta m^2|}{10^{-4} \text{ eV}} \right) \left(\frac{10 \text{ MeV}}{E} \right), \quad (7)$$

where n_e is the electron number density measured in cm^{-3} , N_A is Avogadro's number, θ_V is the neutrino mixing angle in vacuum, $|\Delta m^2|$ is the absolute value of the difference in neutrino masses between two species that are mixing by neutrino oscillations, and E is the neutrino energy.

Figure 8 and Table 10 give the electron number density as a function of solar radius for the Standard solar model (BP2000). A much more extensive numerical file of the electron number density versus radius is available at <http://www.sns.ias.edu/~jnb>; this file contains the computed values of the electron number density at 2493 radial shells.

We see from Figure 8 that for typical values of the neutrino parameters that allow the so-called LMA and SMA MSW solutions which fit all of the currently available solar neutrino data (e.g., Bahcall, Krastev, & Smirnov 1998), the experimentally most important ^8B neutrinos ($E \geq 5$ MeV) satisfy the resonance condition, Eq. (7), at radii that are smaller

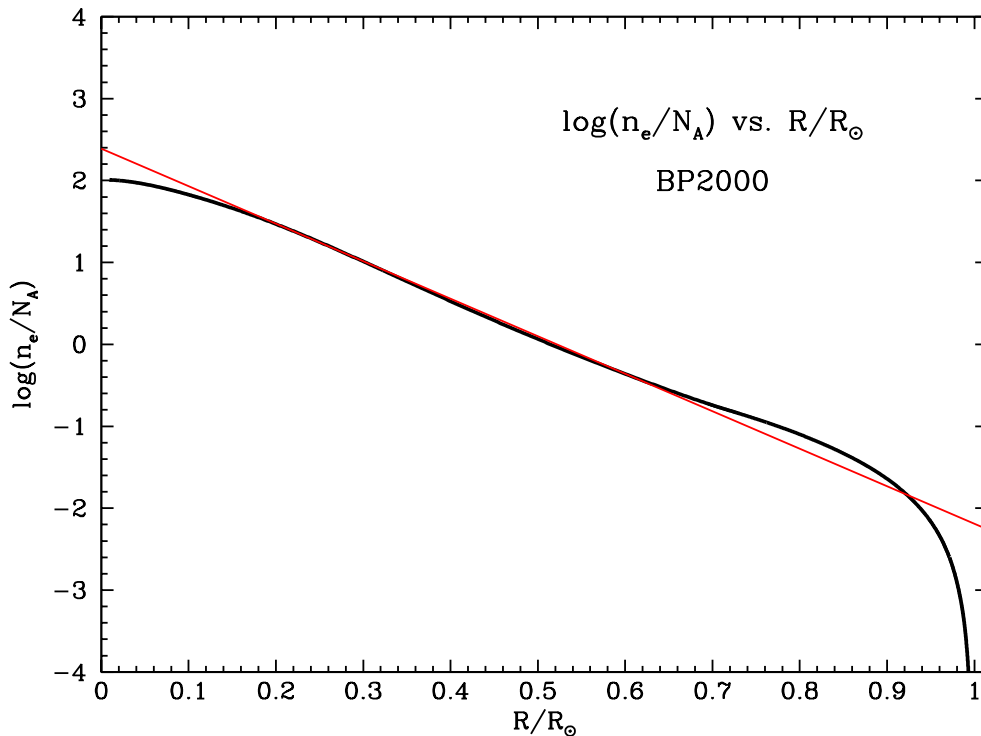


Fig. 8.— The electron number density, n_e , versus solar radius for the Standard solar model (BP2000). The straight-line fit shown in Figure 8 is an approximation, Eq. (8), given by Bahcall (1989). Equation (8) has been used previously in many analyses of matter effects on solar neutrino propagation. Precise numerical values for n_e are available at www.sns.ias.edu/~jnb.

than the radius of the convective zone. For the so-called LOW MSW solutions and for all MSW solutions with $\theta_V \sim \pi/4$, the resonance radius falls in the outer part of the sun.

We have not previously published accurate values for the electron density in the outer parts of the sun, $r \geq 0.8R_\odot$. The straight line in Figure 8 is an approximation to the electron number density in the standard solar model of Bahcall & Ulrich (1988) (see Bahcall 1989). This approximation, which has been used for over a decade by different groups analyzing solar neutrino data, is

$$n_e/N_A = 245 \exp(-10.54R/R_\odot) \text{ cm}^{-3}. \quad (8)$$

Table 10: The electron number density versus radius for the standard solar model. The tabulated values are $\log(n_e/N_A)$, where n_e is measured in number per cm^3 and N_A is Avogadro’s number. A more extensive numerical file of n_e , contain electron number densities at 2493 radial shells, is available at <http://www.sns.ias.edu/~jnb>.

R/R_\odot	$\log(n_e/N_A)$	R/R_\odot	$\log(n_e/N_A)$
0.01	2.008E+00	0.55	-1.527E-01
0.05	1.956E+00	0.60	-3.605E-01
0.10	1.827E+00	0.65	-5.585E-01
0.15	1.662E+00	0.70	-7.428E-01
0.20	1.468E+00	0.75	-9.098E-01
0.25	1.249E+00	0.80	-1.099E+00
0.30	1.012E+00	0.85	-1.330E+00
0.35	7.687E-01	0.90	-1.642E+00
0.40	5.269E-01	0.95	-2.164E+00
0.45	2.914E-01	1.00	-6.806E+00
0.50	6.466E-02		

Figure 8 shows that the approximation given in Eq. (8) fails badly in the outer regions of the sun. Recently, several different analyses have been published using the electron number density shown in Figure 8 (or, more precisely, the computer file for $n_e(r)$ which is available at <http://www.sns.ias.edu/~jnb>).

5.3. Neutrino fluxes as a function of solar age

Figure 9 shows the most important solar neutrino fluxes, the pp , ${}^7\text{Be}$, ${}^8\text{B}$, and ${}^{13}\text{N}$ fluxes, as a function of solar age. The fluxes displayed in the figure were computed using the Standard model and are normalized by dividing each flux by its value at the present epoch, labeled by the word ‘today’ in the figure.

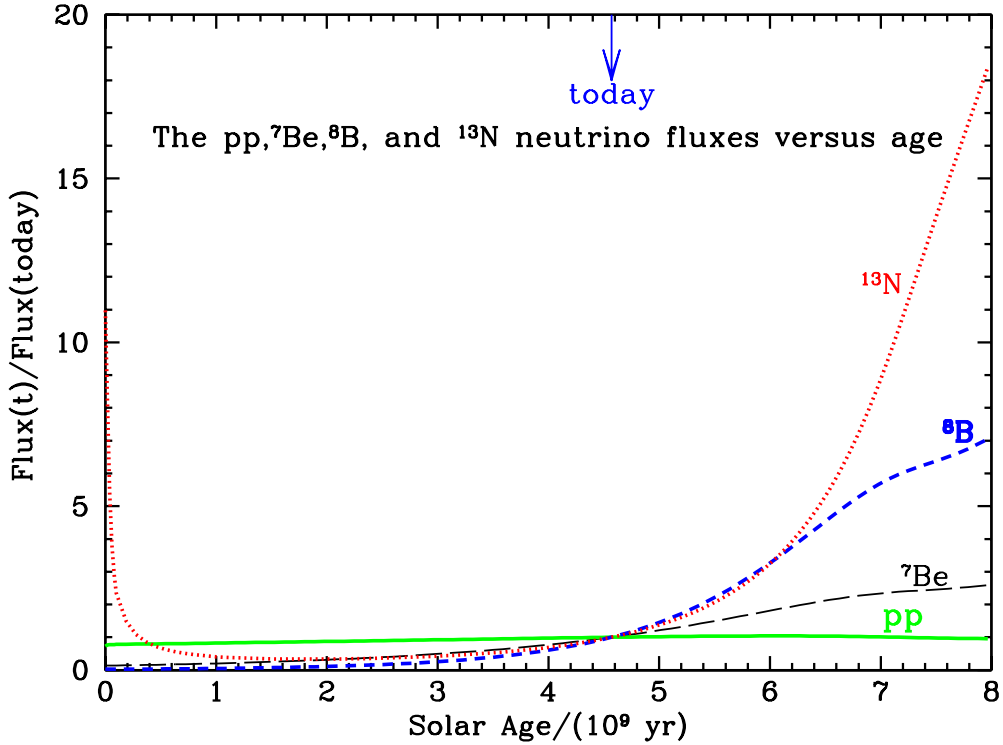


Fig. 9.— The pp , ${}^7\text{Be}$, ${}^8\text{B}$, and ${}^{13}\text{N}$ neutrino fluxes as a function of solar age. The figure shows the Standard model ratios of the fluxes divided by their values at 4.57×10^9 yr. The pp flux is represented by a solid line, the ${}^7\text{Be}$ flux by a line of long dashes, the ${}^8\text{B}$ flux by short dashes, and the ${}^{13}\text{N}$ flux by a dotted line.

The pp flux is relatively constant over the entire 8 billion years show in Figure 9. At the beginning of its lifetime, the pp flux is about 75% of its current value and reaches 90% of its present value after 2.6 billion years. At the current epoch, the flux is changing very slowly, about 4% per billion years. The pp flux reaches a maximum, 4% larger than its current value, at a solar age of 6.0 billion years and then declines slowly and steadily to 96% of its present value at an age of 8 billion years.

The ${}^7\text{Be}$ and ${}^8\text{B}$ neutrino fluxes increase monotonically and by larger amounts than the pp flux. Both the ${}^7\text{Be}$ and the ${}^8\text{B}$ fluxes begin with very low fluxes relative to their current values, 14% and 3%, respectively, of their intensities at 4.57×10^7 yr. At a solar age of 8 billion years, the ${}^7\text{Be}$ neutrino flux is 2.6 times larger than it is today and the ${}^8\text{B}$ neutrino

flux is 7.1 times larger than today. At the current epoch, the ${}^7\text{Be}$ flux is increasing by about 65% per billion years and the ${}^8\text{B}$ flux is increasing faster, about 120% per billion years.

The ${}^{13}\text{N}$ neutrino flux has the most interesting time dependence. In the first 10^8 y on the main sequence, the ${}^{13}\text{N}$ flux is much larger than its current value because ${}^{12}\text{C}$ has not yet been burned to the equilibrium value appropriate for the CNO cycle. The reaction ${}^{12}\text{C}(p, \gamma){}^{13}\text{N}$ occurs relatively often in this early stage of solar evolution and the neutrino flux from ${}^{13}\text{N}$ beta-decay has a peak value of about 11 times its current flux. The minimum ${}^{13}\text{N}$ flux, 33% of its present value, is attained at a solar age of 1.8 billion years. Thereafter, the ${}^{13}\text{N}$ flux increases steadily as the central temperature of the solar model increases and reaches an intensity of 18 times its current value at a solar age of 8 billion years.

6. Sound speeds

Section 6.1 presents a panoramic view of the predicted Standard model sound speeds and compares the observations and the calculations on a scale that is relevant for interpreting solar neutrino experiments. In § 6.2, we compare on a zoomed-in scale the Standard model calculations with the results of six helioseismological measurements. The zoomed-in scale used in this subsection can reveal fractional discrepancies between calculations and observations that are smaller than 0.1%. In § 6.3, we consider a particular solar model that includes rotation in a plausible way. This model smooths the composition discontinuity at the base of the convective zone, which locally improves the agreement with the measured sound speeds but worsens the overall rms agreement (within the uncertainties allowed by input data). For neutrino emission, the predictions of the rotation model are not significantly different from the Standard model predictions.

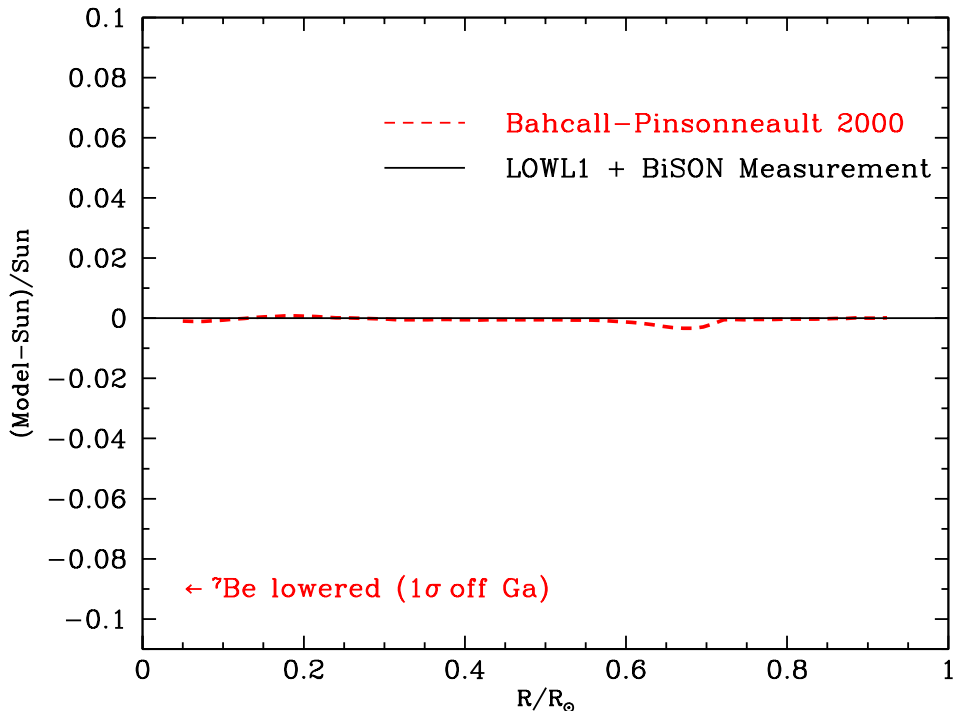


Fig. 10.— Predicted versus measured sound speeds. The figure shows the excellent agreement between the calculated sound speeds for the Standard solar model (BP2000) and the helioseismologically measured (Sun) sound speeds. The horizontal line at 0.0 represents the hypothetical case in which the calculated sound speeds and the measured sound speeds agree exactly everywhere in the sun. The rms fractional difference between the calculated and the measured sound speeds is 0.10% for all solar radii between between $0.05R_{\odot}$ and $0.95R_{\odot}$ and is 0.08% for the deep interior region, $r \leq 0.25R_{\odot}$, in which neutrinos are produced.

6.1. Sounds speeds: panoramic view

Figure 10 shows the fractional differences between the calculated sound speeds for the Standard model and what may be the most accurate available sound speeds measured by helioseismology, the LOWL1 + BiSON Measurements presented in Basu et al. (1997). These sound speeds are derived from a combination of the data obtained by the Birmingham Solar Oscillation Network (BiSON; cf. Chaplin et al. 1996) and the Low- ℓ instrument (LOWL; cf. Tomczyk et al. 1995a,b).

The rms fractional difference between the calculated and the measured sound speeds

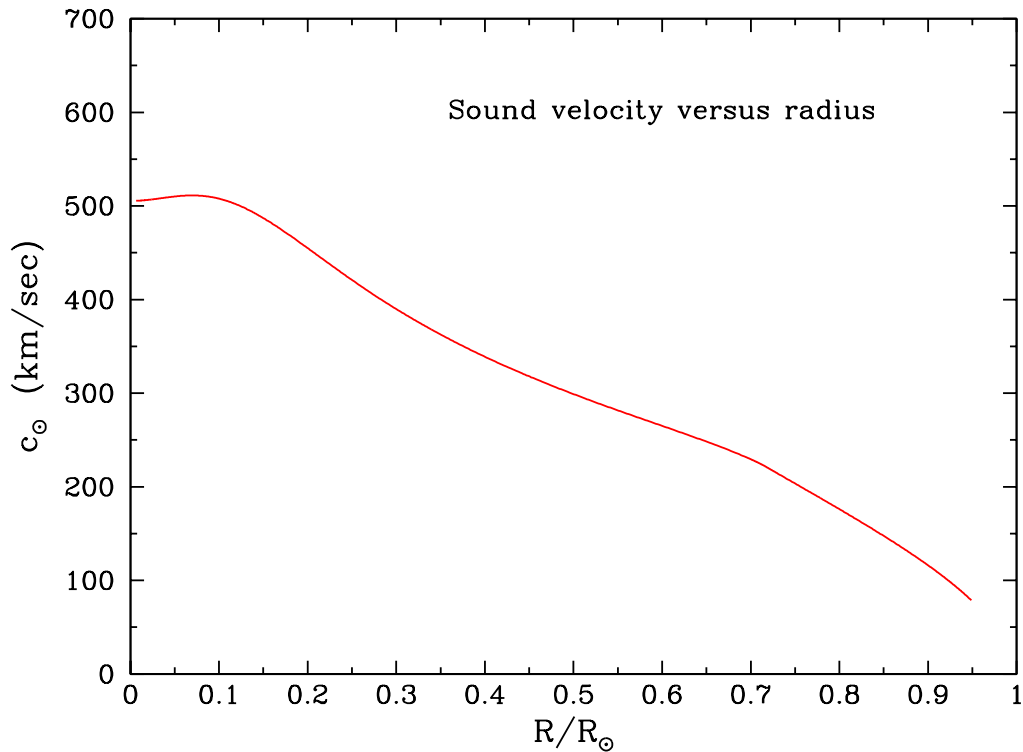


Fig. 11.— The solar sound speed versus the solar radius. The figure shows the calculated solar sound speed versus radius for the standard solar model, Bahcall-Pinsonneault 2000. To an accuracy of about 0.5 km/s the calculated and the observed sound speeds are the same (see Figure 12 and Figure 13).

is 10.4×10^{-4} over the entire region in which the sound speeds are well measured, $0.05R_{\odot} \leq r \leq 0.95R_{\odot}$. In the solar core, $0.05R_{\odot} \leq r \leq 0.25R_{\odot}$ (in which about 95% of the solar energy and neutrino flux are produced in a standard solar model), the rms fractional difference between measured and calculated sound speeds is 6.3×10^{-4} . The Standard model sound speeds agree with the measured sound speeds to 0.1% whether or not one limits the comparison to the solar interior or averages over the entire sun. Systematic uncertainties $\sim 3 \times 10^{-4}$ are contributed to the sound speed profile by each of three sources: the assumed reference model, the width of the inversion kernel, and the measurement errors (see BPB2000).

The vertical scale of Figure 10 was chosen so as to include the arrow marked

“ ${}^7\text{Be}$ lowered (1σ off Ga).” This arrow indicates the typical difference between solar model speeds and helioseismological measurements that would be expected if the discrepancy between the gallium solar neutrino measurements and the predictions in Table 6 were due to errors in the solar physics of the standard solar model (see discussion in BP98).

Figure 11 and Table 11 give the sound speeds versus the solar radius that are calculated using the Standard solar model. The sound speed declines from about 500 km/s in the solar core to about 100 km/s at $0.95R_{\odot}$. An extensive table of the Standard model sound speeds is available at <http://www.sns.ias.edu/~jnb> .

Table 11: The sound speed as a function of radius for the Standard solar model. The Sound speeds are given in units of 100 km/s.

R	c_s	R	c_s
(R_{\odot})	(100 km/s)	(R_{\odot})	(100 km/s)
0.01	5.057	0.50	2.990
0.05	5.101	0.55	2.817
0.10	5.078	0.60	2.651
0.15	4.870	0.65	2.483
0.20	4.550	0.70	2.295
0.25	4.210	0.75	2.035
0.30	3.898	0.80	1.761
0.35	3.627	0.85	1.476
0.40	3.389	0.90	1.162
0.45	3.179	0.95	0.778

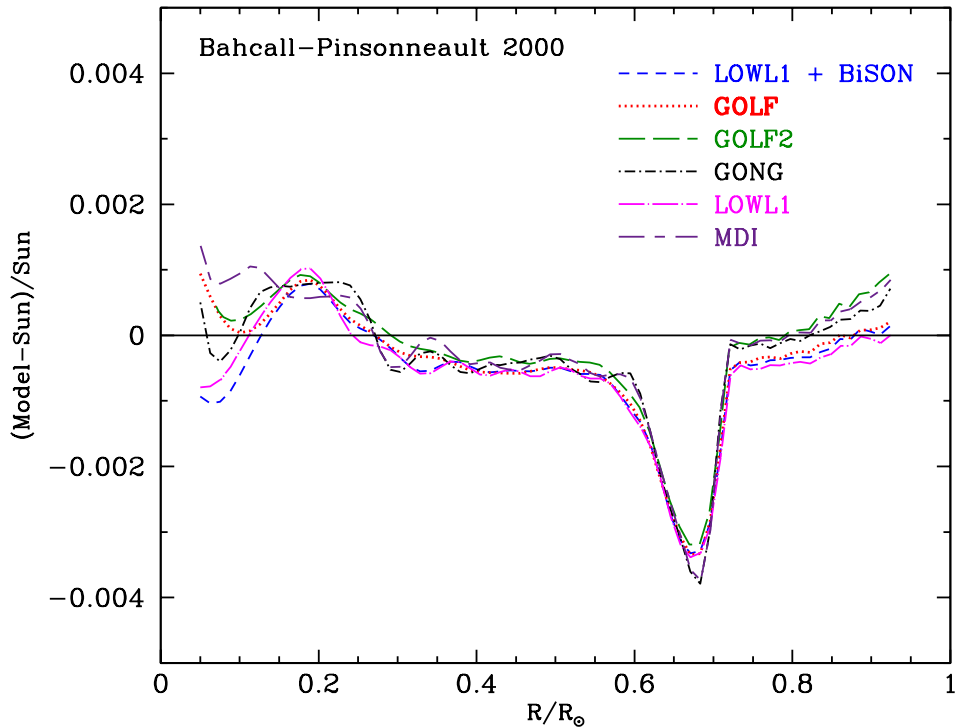


Fig. 12.— Six precise helioseismological measurements versus BP2000. The figure compares the fractional difference between the sound speeds calculated for the Standard solar model (BP2000) and the sound speeds in six helioseismological experiments. The references to the helioseismological data are given in the text. Systematic uncertainties due to the assumed reference model and the width of the inversion kernel are each ~ 0.0003 (see BPB2000).

6.2. Sounds speeds: zoom in

Figure 12 compares the results of six precise observational determinations of the solar sound speed with the results of our Standard solar model. The vertical scale has been expanded by a factor of 21 relative to Figure 10 in order to show the small but robust discrepancies between the calculations and the observations and to indicate the size of the differences between the various measurements. In the deep solar solar interior where neutrinos are produced, $R/R_{\odot} \leq 0.25$, the differences between the various observational determinations of the sound speed are comparable to the differences between BP2000 and any one of the measured sets of sound speeds.

The p -mode frequencies used in deriving the observed sound speeds shown in Figure 12 were obtained from a number of different sources. In addition to the LOWL1 + BiSON data described in § 6.1, we have used data from a number of other sources. (1) Data from the first year of LOWL observations. The sound speed inversions are described in Basu et al. (1996) and are referred to as LOWL1 in this paper. (2) Data from the Michelson Doppler Imager (MDI) instrument on board the Solar and Heliospheric Observatory (SOHO) during the first 144 days of its operation (cf. Rhodes et al. 1997). The results of the sound speed inversions using these data are from Basu (1998). (3) The frequencies obtained from the data obtained by the Global Oscillation Network Group (GONG) between months 4–14 of its observations. The solar sound-speeds are from Basu (1998). (4) Initial observation taken by the Global Oscillations at Low Frequencies (GOLF) instrument on board SOHO, combined with intermediate data from MDI. We have labeled the sound speeds obtained as GOLF1 and the solar sound speed results can be found in Turck Chiéze et al. (1997). (5) More recent data from GOLF (Thierry et al. 2000), combined with intermediate degree data obtained from the first 360 days observations by the MDI instrument (Schou et al. 1997). The sound-speed results are described in Basu et al. (2000). These results have been labeled as GOLF2.

The MDI and GONG sets have good coverage of intermediate degree modes. The MDI set has p -modes from $\ell = 0$ up to a degree of $\ell = 194$ while the GONG set has modes from $\ell = 0$ up to $\ell = 150$. However, both these sets are somewhat deficient in low degree modes. The LOWL1 + BiSON combination, on the other hand, has a better coverage of low degree modes, but has modes from $\ell = 0$ only up to $\ell = 99$. The GOLF data sets only contain low-degree modes ($l = 0, 1, 2$) and hence have to be combined with other data before they can be used to determine the solar sound speed profile.

Figure 13 shows the somewhat less precise agreement that was obtained between BP98

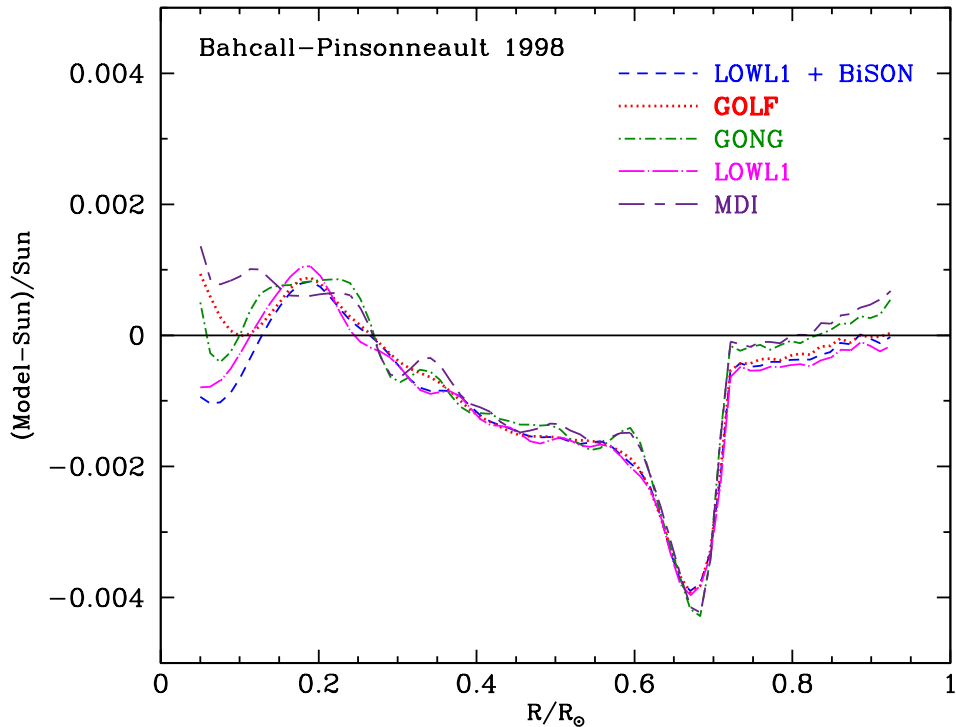


Fig. 13.— Five precise helioseismological measurements versus BP98. The figure compares the fractional difference between the sound speeds calculated for the 1998 Standard solar model (BP98) and the sound speeds in five helioseismological experiments. The references to the helioseismological data are given in the text. (The GOLF2 data were not available when this comparison was originally made.) The rms fractional difference between the calculated and the measured sound speeds is 0.13% for all solar radii between between $0.05R_{\odot}$ and $0.95R_{\odot}$.

(Bahcall, Basu, & Pinsonneault 1998) and the helioseismological data. The BP98 model and the observed sound speeds agree in the solar interior to about the same accuracy as for BP2000 and the observed speeds. However, the BP98 model sound speeds are about 0.1% smaller than the observed speeds in the broad intermediate region between $0.3R/R_{\odot}$ and $0.7R/R_{\odot}$ (cf. Figure 12 and Figure 13). Averaged over the entire region over which good measurements are available, $0.05R_{\odot}$ to $0.95R_{\odot}$, the rms fractional difference between the BP98 model and the LOWL1 + BiSON sound speeds is 13×10^{-4} , which sound be

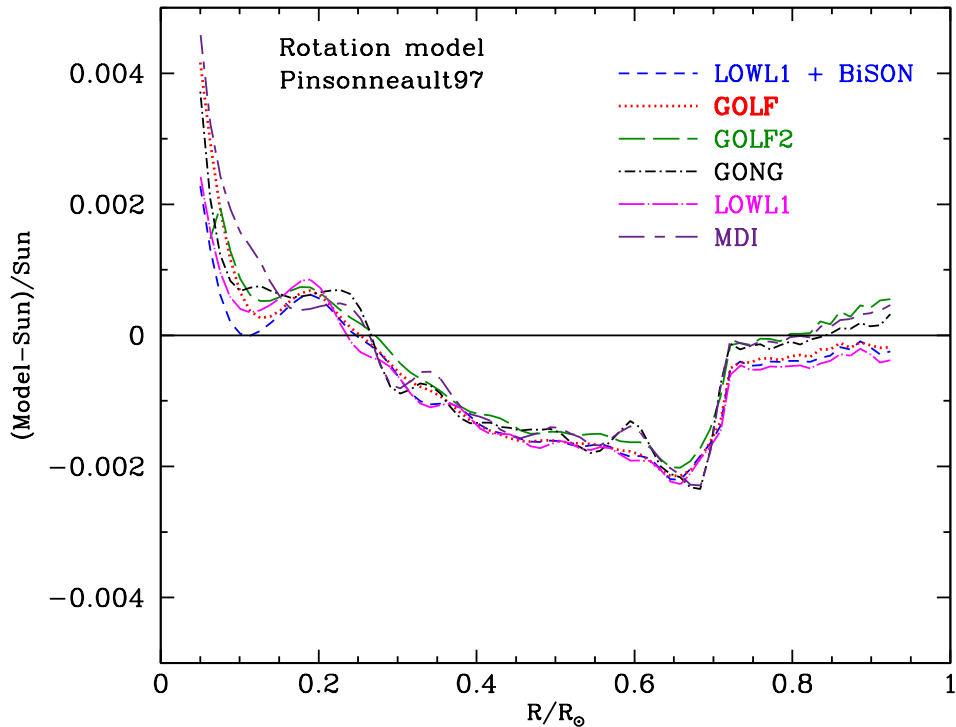


Fig. 14.— Six precise helioseismological measurements versus the Rotation model. The figure compares the fractional difference between the sound speeds calculated for the Rotational solar model and the sound speeds in six helioseismological experiments. The model was developed by Pinsonneault and collaborators to explain the depletion of lithium. The references to the helioseismological data are given in the text.

compared with a rms difference of 10.4×10^{-4} for the BP2000 model (see § 6.1)⁴.

⁴The Standard model described in this paper differs from the BP98 model in two respects, both discussed in Section 2.1, that are significant for helioseismology: the correction of the opacity interpolation error and the slightly different heavy element mixture adopted for the BP2000 model. For helioseismology, the only significant difference between GN93 and BP98 is the correction of the interpolation error; the heavy element abundances used for both models are the same (with $Z/X = 0.0245$). When a figure like Figure 12 was constructed using GN93 instead of BP2000, the general form of the small differences was practically the same. In fact, the rms difference averaged over the whole sun between GN93 and LOWL1

In BP98, we speculated that the broad feature of disagreement at the 0.1% level in Figure 13 might be due to a combination of small errors in the adopted radiative opacities or in the equations of state. We investigated the implications for solar neutrino fluxes of the possibility that the small, broad discrepancy was due to an opacity error and concluded that if this were the case then the corrected solar model would predict ${}^7\text{Be}$ and ${}^8\text{B}$ neutrino fluxes that are about 5% larger than the fluxes predicted by BP98.

Indeed, the origin of the broad discrepancy is due to an error in interpolating the radiative opacity near the edges of the opacity tables, as explained in § 2.1. The effect on the neutrino fluxes is somewhat smaller than we had estimated, an increase (relative to BP98) of 2% for ${}^7\text{Be}$ neutrinos and 3% for ${}^8\text{B}$ (cf. the results for GN93 in Table 6 and Table 1 of BP98).

6.3. Sound speeds: rotation

Figure 14 compares the sound speeds of the Rotation model with the six precise observed sets of sound speeds. In the region between $0.3R_{\odot}$ and $0.6R_{\odot}$, the agreement between the Rotation model and the helioseismological data is slightly less good than with the Standard solar model (compare Figure 12 and Figure 14). Quantitatively, over the entire region between $0.05R_{\odot}$ to $0.95R_{\odot}$, the rms fractional difference between the Rotation model and the LOWL1 + BiSON sound speeds is 12×10^{-4} , which is to be compared with 10×10^{-4} for BP2000. In the solar core ($\leq 0.25R_{\odot}$), the two models, Rotation and BP2000, have almost identical rms fractional differences with respect to the LOWL1 + BiSON sound

+ BiSON is 0.00086, which is slightly better than the value of 0.00104 for BP2000 versus LOWL1 + BiSON. One therefore obtains the correct impression by comparing Figure 12 and Figure 13.

speeds, 0.073% and 0.0064%, respectively.

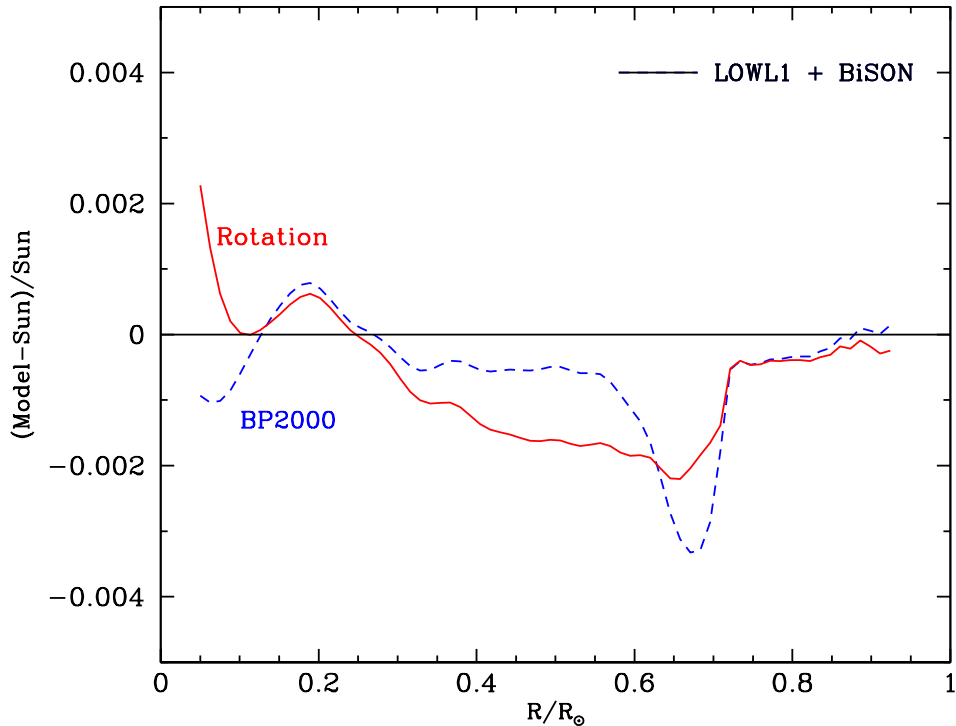


Fig. 15.— BP2000 versus the Rotation model. The figure compares the fractional difference between the sound speeds determined from the LOWL1 + BiSON data with the sound speeds calculated for the BP2000 solar model and the Rotational solar model. The BP2000 model agrees slightly better with the measured sound speeds in the intermediate region between $0.3R_{\odot}$ and $0.6R_{\odot}$.

Figure 15 compares both the Rotation and the Standard model with just the LOWL1 + BiSON sound speeds. This figure shows that the Rotation model gives marginally better agreement with the measured sound speeds right at the base of the convective zone, comparable agreement in the deep interior, $r \leq 0.25R_{\odot}$, and slightly less good agreement in the intermediate region between $0.3R_{\odot}$ and $0.6R_{\odot}$.

The neutrino fluxes calculated with the Rotation model lie well within the estimated errors in the Standard model fluxes, as can be seen easily by comparing the fluxes and the errors given in Table 6 and Table 9. The ${}^7\text{Be}$ flux for the Rotation model is 3% less than the

Standard model ${}^7\text{Be}$ and the ${}^8\text{B}$ flux is 5% lower than the corresponding Standard model value. The Rotation model predicts a capture rate by ${}^{37}\text{Cl}$ that is 0.3 SNU less than the Standard model rate and a ${}^{71}\text{Ga}$ capture rate that is 2 SNU less than the Standard model rate.

7. Helium abundance and depth of the convection zone

Table 12 gives the calculated present-epoch values for the depth of the convective zone, $R(\text{CZ})$, and the surface helium abundance, Y_s , for all 11 of the solar models considered in this paper.

The observed values determined using measurements of p -modes are $R(\text{CZ}) = (0.713 \pm 0.001)R_\odot$ (Basu & Anita 1995; for earlier work see Christensen-Dalsgaard, Gough, & Thompson 1991) and $Y_s = 0.249 \pm 0.003$ (Basu & Anita 1997; see also Richard et al. 1996).

The quoted errors are systematic; the statistical uncertainties are much smaller. For example, the cited uncertainty for Y_s is designed to span the two values obtained when using two different equations of state (cf. Basu & Anita 1997). There is no rigorous way of establishing a confidence level based upon agreement within, for example, one or two times the estimated systematic uncertainty. We point out that the recent reassessment of Z/X by Grevesse and Sauval (1998) resulted in a value of $Z/X = 0.0230$ which differs from the helioseismologically recommended value of $Z/X = 0.0245 \pm 0.0008$ by twice the quoted uncertainty of the helioseismological determination.

As a rule-of-thumb, we shall regard agreement within two times the quoted systematic uncertainty as ‘satisfactory’ and agreement within one times the quoted systematic uncertainty as ‘excellent’.

Table 12: Helium abundance and the depth of the convective zone. The calculated present-day helium abundance on the surface and the convective zone depth are given for 11 solar models discussed in this paper. The quoted errors in the measured values of Y and $R(CZ)$ represent best estimates of the systematic uncertainties but cannot be interpreted rigorously in terms of 1σ or 3σ errors.

Standard	Y_s	$R(CZ)$
Standard	0.244	0.714
NACRE	0.244	0.713
AS00	0.239	0.714
GN93	0.245	0.712
Pre-MS	0.246	0.713
Rotation	0.248	0.714
Radius ₋₇₈	0.245	0.712
Radium ₋₅₀₈	0.245	0.712
No diffusion	0.266	0.726
Old physics	0.248	0.712
$S_{34} = 0$	0.242	0.715
Mixed	0.254	0.732
Measured	0.249 ± 0.003	0.713 ± 0.001

Nine of the eleven solar models considered in this paper give excellent or satisfactory agreement with the observed depth of the convective zone. The only exceptions to the good agreement with the measured convective zone depth are the No Diffusion and the Mixed models, which are both strongly disfavored by the helioseismological measurements.

The No Diffusion, $S_{34} = 0$, and AS00 models are the only ones that are not within twice the quoted uncertainty in the measured surface helium abundance. The No Diffusion model yields a surface helium abundance that is more than five times the quoted uncertainty away from the helioseismological measurement, which very strongly disfavors the No Diffusion

model. The surface helium abundance calculated for the AS00 model is also rather far from the helioseismological value, more than three times the quoted uncertainty in the helioseismological determination. This discrepancy should be examined more fully in future years as the abundance determinations are refined and the helioseismological determination of the helium abundance is repeated and the input data to the helioseismological analysis is varied over a wide range of allowed possibilities.

8. Discussion and summary

This paper provides new information about four topics: 1) the characteristics of the Standard solar model at the current epoch (see § 8.1 below); 2) time dependences of important characteristics of the Standard solar model (§ 8.2); 3) neutrino fluxes and related quantities for standard and variant solar models (§ 8.3); and 4) measured versus calculated solar sound speeds (§ 8.4). Extensive numerical data that are useful for applications are available at <http://www.sns.ias.edu/~jnb> .

Just for fun, we provide our favorite list, our “top three,” among the many disparate results presented in this paper. Our top three results are listed in § 8.5.

8.1. Standard solar model: current epoch

We present detailed numerical tabulations of the computed characteristics of our Standard solar model, which is defined and discussed in § 2. These tables include, as a function of the solar radius, the enclosed mass fraction, the temperature, mass density, electron number density, the pressure, and the luminosity fraction created in a given spherical shell, as well as the mass fractions of ^1H , ^3He , ^4He , ^7Be , ^{12}C , ^{14}N , and ^{16}O . Over the years, previous numerical versions of our Standard model have been used for

a variety of purposes that range from comparisons with other stellar evolution codes, estimating the importance in the sun of newly considered physical effects, searching for possible instabilities in the sun, comparison with helioseismological measurements, and the calculation of processes (especially the MSW effect) that influence the propagation of solar neutrinos.

In the past, we have published in hard copy form increasingly more detailed and precise numerical tables of the characteristics of the solar interior. The capabilities of current calculations and the requirements of some of the most interesting applications have made complete hard copy publication no longer appropriate. We have therefore limited ourselves in § 2 to describing briefly the ingredients we use in calculating the current Standard model. We present the numerical results in exportable data files that are available at <http://www.sns.ias.edu/~jnb> .

8.2. Standard solar model: time dependences

For the first time in this series of papers, we have focused, especially in § 3, on details of the time dependence of important characteristics of the Standard solar model. We find some simple scaling relations. For example, the solar luminosity, $L_{\odot}(t)$, is approximately related to the solar radius, $R_{\odot}(t)$, as $L_{\odot}(t) \propto R_{\odot}(t)^{2.5}$. The depth of the convective zone, $R(\text{CZ}, t)$, scales as $R(\text{CZ}, t) \propto R_{\odot}(t)$, and the central temperature, $T_c(t)$, shows a similar behavior, $T_c(t) \propto R_{\odot}(t)$. Moreover, we find that the mass of the convective zone, $M(\text{CZ}, t)$ satisfies $M(\text{CZ}, t) \propto R_{\odot}(t)^{-2}$. The effective temperature is approximately constant, varying by only $\pm 0.7\%$ from a solar age of 2 billion years to 8 billion years.

These results make predictions that are potentially testable. For example, the measurement of the luminosity (by astrometry) of a star with the same mass and chemical

composition (Z/X) as the sun would determine the star’s age and allow us to predict the star’s effective temperature and the depth and mass of the convective zone. In a future publication, we hope to explore the extent to which the results found here for the temporal evolution depend upon the precise value of the stellar mass and the initial composition ratio, Z/X .

The predicted time evolution of the solar luminosity is robust. Figure 2 shows that all solar models, even those models with deficient physics that are strongly disfavored by helioseismological measurements, predict essentially the same luminosity evolution. The total luminosity in the Standard model increases by 48% from the zero-age main sequence stage to the present epoch. This prediction is a constraint on models for the evolution of the earth.

We have presented in § 3 the time evolution of some of the principal physical quantities characterizing the solar core (the central temperature, density, pressure, and hydrogen mass fraction, as well as the fractions of the solar luminosity generated by different nuclear reactions). We also present the evolution of important quantities at the base of the convective zone (radiative opacity, temperature, density, and pressure). We hope that these data and the scaling relations we have inferred will be sufficient to permit a future physical understanding of the time dependences using analytic and semi-analytic arguments.

8.3. Neutrino fluxes and related quantities

Table 6 presents the neutrino fluxes and the event rates in the chlorine, gallium, lithium, and electron-scattering neutrino experiments that are predicted by the Standard solar model. These predictions assume that nothing happens to solar neutrinos after they are produced. The table also gives estimates of the uncertainties in the fluxes and the event

rates; § 5.1 contains a discussion of the physical origin of the uncertainties, as well as the software used to calculate the asymmetric error estimates.

How do the predictions of solar neutrino event rates compare with experiment? Table 7 compares the predictions of BP2000 with the results of the chlorine, GALLEX + GNO, SAGE, Kamiokande, and Super-Kamiokande solar neutrino experiments. This table assumes nothing happens to the neutrinos after they are created in the sun. The standard predictions differ from the observed rates by many standard deviations. Because of an accidental cancellation, the predicted solar neutrino event rates for BP2000 and BP98 are almost identical (see Section 5.1.1).

Table 9 compares the neutrino fluxes and the experimental event rates for all nine of the solar models whose helioseismological properties were investigated in BP2000, plus two additional standard-like models considered here which have somewhat different heavy-element to hydrogen ratios. The seven standard-like models (the first seven models in Table 9) all produce essentially the same neutrino predictions; the spreads in the predicted pp , ${}^7\text{Be}$, and ${}^8\text{B}$ fluxes are $\pm 0.7\%$, $\pm 3\%$, and $\pm 6.5\%$, respectively. The calculated rates for the seven standard-like solar models have a range of ± 0.45 SNU for the chlorine experiment and ± 2 SNU for the gallium experiments.

The estimated total errors from external sources (see Table 6), such as nuclear cross section measurements and heavy element abundances, are about a factor of three larger than the uncertainties resulting from the solar model calculations.

We have investigated one possible source of systematic errors, the relative weights assigned to different determinations of nuclear fusion cross sections. We calculated the neutrino fluxes and predicted event rates using the NACRE (Angulo et al. 1999) fusion cross sections rather than the Adelberger et al. (1998) cross sections. All changes in fluxes and predicted event rates between the NACRE predictions and the Standard predictions

are much less than the 1σ uncertainties quoted for the Standard model (cf. Table 6 and Table 8).

The neutrino event rates predicted by all seven of the standard-like solar models considered here are inconsistent at the 5σ level (combined theoretical and experimental errors) with the results of the two gallium experiments, GALLEX and SAGE, assuming no new physics is occurring. The inconsistency with the chlorine experiment is similar but more complex to specify, since the largest part of the theoretical uncertainty in the calculated standard capture rate is due to the electron-type neutrinos from ^8B beta-decay. The fractional uncertainty in the ^8B flux depends upon the magnitude of the flux created in the solar interior. Moreover, the amount by which this ^8B flux is reduced depends upon the adopted particle physics scenario.

A similar level of inconsistency persists even for the ad hoc deficient models, such as the $S_{34} = 0$ and Mixed models, that were specially concocted to minimize the discrepancy with the neutrino measurements. For example, the calculated rates for the Mixed model are $6.15^{+1.0}_{-0.85}$ SNU for the chlorine experiment and $115^{+6.8}_{-5.1}$ SNU for gallium experiments. The Mixed model is 4.2σ below the measured chlorine rate and 6.3σ below the measured gallium rate. In addition, the deficient models are strongly disfavored by the helioseismology measurements.

Figure 9 shows the calculated time dependence of the pp , ^7Be , ^8B , and ^{13}N solar neutrino fluxes. At the current epoch, the pp flux is increasing at a rate of 4% per billion years, and the ^7Be , ^8B , and ^{13}N fluxes at the rates of 45%, 90%, and 99% per billion years, respectively. Since the age of the sun is estimated to be uncertain by only 5×10^{-3} billion years (see the Appendix by Wasserburg in Bahcall & Pinsonneault 1995), the age of the sun does not represent a significant uncertainty for solar neutrino predictions.

Figure 8 and Table 10 give the electron number density as a function of position in the

sun for the Standard solar model. The distribution of the electron density is required to compute the probability for matter-induced neutrino oscillations. We have not previously published precise values for the electron number density in the outer regions of the sun; the outer regions are relevant for large mixing angle neutrino oscillations with relatively low neutrino mass differences ($\Delta m^2 < 10^{-8} \text{eV}^2$).

8.4. Sound speeds

Figure 10 shows the excellent agreement between the helioseismologically determined sound speeds and the speeds that are calculated for the Standard solar model. The scale on this figure was chosen so as to highlight the contrast between the excellent agreement found with the Standard model and the two orders of magnitude larger rms difference for a solar model that could reduce significantly the solar neutrino problems. One would expect characteristically a 9% rms difference between the observations and the predictions of solar models that significantly reduce the conflicts between solar model measurements and solar model predictions. Averaged over the entire sun, the rms fractional difference is only 0.10% between the Standard solar model sound speeds and the helioseismologically-determined sound speeds. The agreement is even better, 0.06%, in the interior region in which the luminosity and the neutrinos are produced. Table 11 presents numerical values for the sound speeds predicted by the Standard solar model at representative radial positions in the sun.

All eight of the standard-like solar models considered in this paper give acceptable agreement with the measured depth of the convective zone and the surface helium abundance (see Table 12). Of the twelve Standard, standard-like, variant, and deviant solar models considered here, only the No Diffusion and Mixed models disagree strongly with the measured convective zone depth.

There are small but robust discrepancies between the measured and the calculated solar sound speeds. Figure 12 shows the fractional differences between the Standard model sound speeds and the speeds measured in each of six different determinations (using p -mode data from LOWL1, BiSON, GONG, MDI, GOLF, and GOLF2). The vertical scale for Figure 12 is expanded 21 times compared to the vertical scale of Figure 10. As can be seen from Figure 12, the differences between observed and measured sound speeds are comparable over much of the sun to the differences between different measurements of the sound speed, but there is a clear discrepancy near the base of the convective zone that is independent of which observational data set is used. There may also be a less prominent discrepancy near $0.2R_{\odot}$.

The agreement between the BP2000 sound speeds and the measured values is improved over what was found earlier with the BP98 model. This improvement may be seen by comparing Figure 12 and Figure 13. The improvement is striking in the region between $0.3R_{\odot}$ and $0.7R_{\odot}$ and is due to the correction of an error in the interpolation algorithm for the radiative opacity (cf. discussion in § 2.1).

The Rotation model includes a prescription for element mixing that was designed to explain the depletion of lithium. The calculated differences between the Rotation and the Standard models represent a reasonable upper limit to the effects that rotation, sufficient to explain lithium depletion, might produce. The overall agreement between the sound speeds of the Rotation model and the helioseismologically determined sound speeds is slightly worse, 0.12% rather than 0.10%, than the agreement obtained with the Standard solar model. The differences between the solar neutrino fluxes predicted between the Rotation model and the Standard model is typically about $0.3\sigma_{\nu}$, where σ_{ν} represents the uncertainties given in Table 6 for the Standard model neutrino fluxes. We conclude that further improvements of the theoretical calculations motivated by refinements of p -mode

oscillation measurements are unlikely to significantly affect the calculated solar neutrino fluxes.

8.5. Top three results

Here are our favorite three results in this paper.

- The robust luminosity evolution of the sun (see Figure 2).
- The excellent agreement of the Standard model sound speeds with the measured sound speeds on the scale relevant for solar neutrino discussions (see Figure 10).
- The simple relations as a function of time between the solar radius, the solar luminosity, the depth of the convective core, and the mass of the convective core (see Eq. 1–Eq. 5).

We are grateful to many colleagues in solar physics, nuclear physics, and particle physics for valuable discussions, advice, criticism, and stimulation. JNB is supported in part by an NSF grant #PHY-0070928.

REFERENCES

- Abdurashitov, J. N. et al. (SAGE Collaboration) 1999, *Phys. Rev. C*, 60, 055801
- Adelberger, E. C. et al. 1998, *Rev. Mod. Phys.*, 70, 1265
- Alexander, D. R., & Ferguson, J. W. 1994, *ApJ*, 437, 879
- Angulo, C. et al. 1999, *Nucl. Phys. A*, 656, 3
- Antia, H. M. 1998, *A&A*, 330, 336
- Asplund, M. 2000, *Astron. & Astrophys.* (in press), astro-ph/0005322.
- Bahcall, J. N. 1989, *Neutrino Astrophysics* (Cambridge: Cambridge University Press).
- Bahcall, J. N. 1994, *Phys. Rev. D*, 49, No. 8, 3923
- Bahcall, J. N. 1997, *Phys. Rev. C*, 56, No. 6, 3391
- Bahcall, J. N., Bahcall, N. A., & Shaviv, G. 1968, *Phys. Rev. Lett.* 20, 1209
- Bahcall, J. N., Basu, S., & Pinsonneault, M. H. 1998, *Phys. Lett. B*, 433, 1
- Bahcall, J. N., Fowler, W. A., Iben, I., & Sears, R. L. 1963, *ApJ*, 137, 344
- Bahcall, J. N., & Glasner, A. 1994, *ApJ*, 427, 485
- Bahcall, J. N., Huebner, W. F., Lubow, S. H., Parker, P. D., & Ulrich, R. K. 1982, *Rev. Mod. Phys.*, 54, 767
- Bahcall, J. N., Krastev, P. I., & Smirnov, A. Yu. 1998, *Phys. Rev. D*, 58, 096016-1
- Bahcall, J. N., Lisi, L., Alburger, D. E., De Braekeleer, L., Freedman, S. J., & Napolitano, J. 1996, *Phys. Rev. C*, 54, 411

- Bahcall, J. N., & Pinsonneault, M. P. 1992, *Rev. Mod. Phys.*, 64, 885
- Bahcall, J. N., & Pinsonneault, M. H. 1995, *Rev. Mod. Phys.*, 67, 781
- Bahcall, J. N., & Ulrich, R. K. 1988, *Rev. Mod. Phys.*, 60, 297
- Basu, S. 1998, *MNRAS*, 298, 719
- Basu, S. & Antia, H. M. 1995, *MNRAS*, 276, 1402
- Basu, S. & Antia, H. M. 1997, *MNRAS*, 287, 189
- Basu, S., et al. 1997, *MNRAS*, 292, 243
- Basu, S., Pinsonneault, M. H., & Bahcall, J. N. 2000, *ApJ*, 529, 1084
- Belotti, E. et al. (GNO Collaboration), proceedings of the XIX International Conference on Neutrino Physics & Astrophysics, Sudbury, Canada, June 16–21, 2000.
- Brown, T. M., & Christensen-Dalsgaard, J. 1998, *ApJ*, 500, L195
- Chaplin et al. 1996, *Solar Phys.*, 168, 1
- Christensen-Dalsgaard, J., Gough, D. O., & Thompson, M. J. 1991, *ApJ*, 378, 413
- Cleveland, B. T., Daily, T., Davis, R., Jr., Distel, J. R., Lande, K., Lee, C. K., Wildenhain, P. S. & Ullman, J. 1998, *ApJ*, 496, 505
- Cumming, A., & Haxton, W. C. 1996, *Phys. Rev. Lett.*, 77, 4286
- Davis, R. 1994, *Prog. Part. Nucl. Phys.*, 32, 13
- Davis, R., Jr., Harmer, D. S., & Hoffman, K. C. 1968, *Phys. Rev. Lett.*, 20, 1205
- Fukuda, Y. et al. (Kamiokande Collaboration) 1996, *Phys. Rev. Lett.*, 77, 1683

- Fukuda, Y. et al. (Super-Kamiokande Collaboration) 1998, *Phys. Rev. Lett.*, 81, 1158;
erratum, 81, 4279
- Gavrin, V. (SAGE Collaboration), proceedings of the XIX International Conference on
Neutrino Physics & Astrophysics, Sudbury, Canada, June 16–21, 2000.
- Grevesse N., & Noels A. 1993, in *Origin and Evolution of the Elements*, ed. N. Prantzos, E.
Vangioni-Flam, & M. Cassé, (Cambridge: Cambridge University Press), 15
- Grevesse, N. & Sauval, A. J. 1998, *Space Sci. Rev.*, 85, 161
- Gruzinov, A., & Bahcall, J. N. 1998, *ApJ*, 504, 996
- Guenther, D. B., Demarque, P., Kim, Y.-C., & Pinsonneault, M. H. 1992, *ApJ*, 387, 372
- Hampel, W. et al. (GALLEX Collaboration) 1999, *Phys. Lett. B*, 447, 127
- Iben, I. 1965, *ApJ*, 141, 933
- Iglesias, C. A., & Rogers, F. J. 1996, *ApJ*, 464, 943
- Iglesias, C. A., Rogers, F. J., & Wilson, B. G. 1992, *ApJ*, 397, 717
- Kurucz, R. L. 1991, in *NATO ASI Series, Stellar Atmospheres: Beyond Classical Models.*,
ed. L. Crivellari, I. Hubeny, & D. G. Hummer (Dordrecht: Kluwer) 441
- Lande, K. (Homestake) 2000, proceedings of the XIX International Conference on Neutrino
Physics & Astrophysics, Sudbury, Canada, June 16–21, 2000.
- Leibacher, J. W., & Stein, R. F. 1971, *ApJ*, 7, L191
- Marcucci, L. E., Schiavilla, R., Viviani, M., Kievsky, A., & Rosati, S. 2000a, *Phys. Rev.*
Lett., 84, 5959

- Marcucci, L. E., Schiavilla, R., Viviani, M., Kievsky, A., Rosati, S., & Beacom, J. F. 2000b, nucl-th/0006005
- Mikheyev, S. P., & Smirnov, A. Yu. 1985, Sov. J. Nucl. Phys., 42, 913
- Morel, P., Provost, J., & Berthomieu, G. 2000, A&A, 353, 771
- Pinsonneault, M. H. 1997, ARA&A, 35, 557
- Pinsonneault, M. H., Steigman, G., Walker, T. P., & Narayanan, V. K. 1999, ApJ (in press, astro-ph/980373)
- Pontecorvo, B. 1968, Sov. Phys. JETP, 26, 981
- Proffitt, C. R. 1994, ApJ, 425, 849
- Rhodes, E. J., Jr., Kosovichev, A. G., Schou, J., Scherrer, P. H., & Reiter, J. 1997, Solar Phys., 175, 287
- Richard O., Vauclair S., Charbonnel C., & Dziembowski, W. A. 1996, A&A, 312, 1000
- Rogers, F. J., Swenson, F. J., & Iglesias, C. A. 1996, ApJ, 456, 902
- Salpeter, E. E. 1954, Australian J. Phys., 7, 373
- Schou, J., Kosovichev, A. G., Goode, P. R., & Dziembowski, W. A. 1997, ApJ, 489, L197
- Suzuki, Y. 2000, to appear in the Proceedings of the XIX International Conference on Neutrino Physics & Astrophysics, Sudbury, Canada, June 16–21, 2000 (Amsterdam: Elsevier Science Publishers)
- Thierry et al. 2000, A&A, 355, 743
- Thoul, A. A., Bahcall, J. N., & Loeb, A. 1994, ApJ, 421, 828

Tomczyk, S., Schou, J., & Thompson, M. J. 1995a, ApJ, 448, L47

Tomczyk, S., Streater, K., Card, G., Elmore, D., Hull, H. & Cacciani, A. 1995b, Solar Phys., 159, 1

Turck Chièze, S. et al. 1997, Solar Phys., 175, 247

Ulrich, R. K. 1970, ApJ, 162, 993

Weiss, A. & Schlattl, H. 1998, A&A, 332, 215

Wolfenstein, L. 1978, Phys. Rev. D, 17, 2369